Bioactive Materials 49 (2025) 437–455

Contents lists available at ScienceDirect

Bioactive Materials

journal homepage: www.keaipublishing.com/en/journals/bioactive-materials

# Protein to biomaterials: Unraveling the antiviral and proangiogenic activities of Ac-Tβ$_{1-17}$ peptide, a thymosin β4 metabolite, and its implications in peptide-scaffold preparation

Khandoker Asiqur Rahaman [a,1], Md Sofequl Islam Mukim [c,e,1], Md Lemon Hasan [a,d], Hyeok Kim [a], Cheol-Ho Pan [c,e], Oh-Seung Kwon [b,d,*], Dae-Geun Song [c,e,**], Hyung-Seop Han [a,d,f,***]

[a] Center for Biomaterials, Korea Institute of Science and Technology, Seoul, 02792, Republic of Korea
[b] Doping Control Center, Korea Institute of Science and Technology, Seoul, 02792, Republic of Korea
[c] Center for Natural Product Systems Biology, KIST Gangneung Institute of Natural Products, Gangneung, 25451, Republic of Korea
[d] Division of Bio-Medical Science & Technology, University of Science and Technology (UST), 113 Gwahangno, Yuseong-gu, Daejeon, 34113, Republic of Korea
[e] Natural Product Applied Science, KIST School, University of Science and Technology (UST), Gangneung, 25451, Republic of Korea
[f] Research and Development Center, Elecell Corporation, Seoul, 02455, Republic of Korea

ARTICLE INFO

*Keywords:*
Thymosin β4
Peptide metabolites
Ac-Tβ$_{1-17}$ peptide
Antiviral peptide
Peptide-based biomaterial
Regenerative medicine

ABSTRACT

Peptide metabolites are emerging biomolecules with numerous possibilities in biomaterial-based regenerative medicine due to their inherent bioactivities. These small, naturally occurring compounds are intermediates or byproducts of larger proteins and peptides, and they can have profound effects, such as antiviral therapeutics, proangiogenic agents, and regenerative medicinal applications. This study is among the first to focus on using thymosin β4 protein-derived metabolites to pioneer novel applications for peptide metabolites in biomaterials. This study found that the novel peptide metabolite acetyl-thymosin β4 (amino acid 1–17) (Ac-Tβ$_{1-17}$) exhibited significant protease inhibition activity against SARS-CoV-2, surpassing its precursor protein. Additionally, Ac-Tβ$_{1-17}$ demonstrated beneficial effects, such as cell proliferation, wound healing, and scavenging of reactive oxygen species (ROS) in human umbilical vein endothelial cells (HUVEC). Integrating Ac-Tβ$_{1-17}$ into a peptide-based scaffold facilitated cell growth and angiogenesis inside the scaffold and through gradual release into the surrounding environment. The Ac-Tβ$_{1-17}$ peptide treatment induced significant biochemical responses in HUVEC, increasing Akt, ERK, PI3K, MEK, and Bcl-2 gene expression and proangiogenic proteins. Ac-Tβ$_{1-17}$ peptide treatment showed similar results in ex vivo by enhancing mouse fetal metatarsal growth and angiogenesis. These findings highlight the potential of natural protein metabolites to generate biologically active peptides, offering a novel strategy for enhancing biomaterial compatibility. This approach holds promise for developing therapeutic biomaterials using peptide metabolites, presenting exciting prospects for future research and applications.

## 1. Introduction

Small proteins and peptides play crucial roles in numerous biological processes in the human body [1]. They can be used as biologically active biomaterials and as therapeutic agents to treat various conditions [2]. By exploring their roles in physiological processes, the functions of proteins and peptides can be understood both scientifically and practically. Acetyl-thymosin β4 (Ac-Tβ4) is a relatively small protein composed of 43 amino acids, widely distributed in the human body [3]. Its biological activity is closely associated with specific amino acid fragments [4], making it a significant research subject in numerous therapeutic developments [5,6]. In addition, recent studies have

Peer review under the responsibility of KeAi Communications Co., Ltd.
* Corresponding author. Doping Control Center, Korea Institute of Science and Technology, Seoul, 02792, Republic of Korea.
** Corresponding author. Center for Natural Product Systems Biology, KIST Gangneung Institute of Natural Products, Gangneung, Republic of Korea.
*** Corresponding author. Center for Biomaterials, Korea Institute of Science and Technology, Seoul, 02792, Republic of Korea.
*E-mail addresses:* oskwon@kist.re.kr (O.-S. Kwon), dsong82@kist.re.kr (D.-G. Song), hyuhan@kist.re.kr (H.-S. Han).
[1] Both authors contributed equally.

https://doi.org/10.1016/j.bioactmat.2025.02.008
Received 28 July 2024; Received in revised form 20 January 2025; Accepted 4 February 2025

highlighted the antiviral potential of Ac-Tβ4 in COVID-19, with promising results advancing the peptide to phase I of drug development as a potential therapeutic agent [7].

SARS-CoV-2, responsible for the COVID-19 pandemic, has caused devastating global health and societal challenges [8]. It relies on two key proteases for replication: the main protease ($M^{pro}$) and papain-like protease. $M^{pro}$ is a crucial CoV-2 protease that controls viral replication. Therefore, $M^{pro}$ has become increasingly appealing as a target for SARS-CoV-2 therapeutic research [9]. It is uniquely specific to peptides, such as $M^{pro}$ cleavage after cleaving glutamine molecules in a polypeptide [10], making it an exciting target for peptide-based drugs. Small bioactive peptides can be engineered as antiviral agents and tailored to specific targets [11]. Currently, numerous peptide-based vaccines [12], immunomodulatory [13], anti-inflammatory [14], and antiviral peptides that act as a SARS-CoV-2 entrance inhibitor have been developed [15,16]. However, owing to the limited availability of antiviral therapies to treat infections arising from challenges such as narrow spectrum [17], drug resistance, side effects, toxicity, and SARS-CoV-2 strain variation [18], the development of specialized antiviral peptides is necessary [19]. Recently, one study reported iteratively de novo-designed tetrapeptides, which were screened using the SARS-CoV-2 mouse model. The inhibitory activity against $M^{pro}$ thus can be used as a valuable screening tool for various peptide fragments as a primary investigation [11].

In recent years, peptide-based biomaterials have garnered attention in the fields of tissue engineering and regenerative medicine [20]. Peptides with biological activities can be incorporated inside or outside a biomaterial to enhance biological activity such as cell growth, proliferation, and angiogenesis [2]. Biomaterials with proangiogenic properties are crucial for rapid recovery following surgical procedures [21]. Proangiogenic materials effectively heal wounds [22], protect against ischemia, and preserve cardiac functions [23]. Pro-angiogenic peptides are promising alternatives to growth factors [24]. These molecules show great potential in drug discovery, as they feature robust and cheap synthetic methodologies for their preparation and improved safety and efficacy profiles [25]. Therefore, pro-angiogenic peptides represent a valuable alternative to traditional drugs for treating cardiovascular diseases and regenerative medicine [26]. Incorporating these materials can significantly enhance the patient outcomes and effectiveness of medical interventions [27].

Our previous study assessed Tβ4 metabolism using commercially available purified enzymes [28], both in vitro and in vivo [29], and identified six metabolite structures. Additionally, we reported a study of TB-500 peptide and its metabolites, which exhibited superior biological effects in primary screening than their parents [30]. Through literature review, we observed that the Ac-Tβ4 protein sequence is hypothetically fragmented and screened for various biological effects by numerous research groups. We have compiled an updated list of Ac-Tβ4 fragments and their corresponding biological effects (Table S1). Numerous peptide drug candidates remain unproven in in vivo or in clinical trials owing to the toxic effects of novel synthetic peptides. Biologically derived protein metabolites offer a safer approach to generating novel peptide fragments. This study assesses the potential of Ac-Tβ4 metabolites, generated in vivo, in vitro, or from commercially available purified enzymes, to produce novel biologically active peptide fragments. We explored antiviral and proangiogenic activities of peptide metabolites in various in vitro and ex vivo experimental models. Additionally, we assess whether the application of these metabolites can enhance the biological effects of other biomaterials tested in the scaffolds. Finally, this study offers a practical application of protein-derived metabolites as a biomaterial, potentially revolutionizing the field of biomaterial development.

## 2. Materials and methods

### 2.1. Chemicals and reagents

All standard peptides were synthetically ordered from A&PEP for use as authentic standards and screening biological activities (Cheongju-si, South Korea). For in vitro experiments, we used mouse embryonic fibroblast cell lines (NIH/3T3) and HUVECs from ATCC (Manassas, VA, USA). Endothelial Cell Growth Medium-2 BulletKit (EGM™-2) was obtained from Lonza (Basel, Switzerland), and Dulbecco's Modified Eagle Medium (DMEM) was purchased from Gibco (Seoul, South Korea). High-performance liquid chromatography (HPLC) grade water was purchased from Merck (Darmstadt, Germany). Methanol and acetonitrile (ACN) (HPLC grade >99 %) were obtained from J.T. Baker (Radnor, PA, USA). Formic acid (FA) was purchased from Sigma-Aldrich (St. Louis, MO, USA). Bicinchoninic acid (BCA) Protein Assay Kits were obtained from Thermo Fisher (Korea, South Korea). All other chemicals were of HPLC analytical grade.

### 2.2. Analysis of the peptide fragments using liquid chromatography-tandem mass spectrometry (LC-MS/MS)

For these experiments, a Shimadzu liquid chromatography instrument was coupled with a Q-Exactive MS/MS device (Thermo Fisher Scientific, San Jose, CA, USA). An ACE C18 column was used for separation (100 × 2.1 mm, 5 μm; Advanced Chromatography Technologies, Aberdeen, UK), and the column temperature was fixed at 35 °C for compound separation. The injection volume was 5 μL, with a flow rate of 0.3 mL/min. We used 0.1 % FA in distilled water as mobile phase A and 0.1 % in methanol as mobile phase B. The mobile phase was as follows: phase B was held at 2 % for 0.05 min, increased from 2 to 95 % over 28 min, held at 95 % for 1 min, and returned to 2 % at 29.01 min, and the process was completed at 30.01 min.

Detection was performed in the positive ionization mode on an Orbitrap mass spectrometer (Q-Exactive, Thermo Fisher Scientific), with full-scan and data-dependent MS/MS scan modes operating under the same conditions to acquire the desired data. The full-scan range was 150–600 *m/z* that was acquired in the profile mode at a resolution of 70,000 (full scan) and 17,500 (dd-MS/MS). All compounds underwent dissociation in the high-energy collision dissociation mode, with a normalized collision energy of 30 eV and an isolation width of 2 *m/z*. The maximum injection time (IT) was 100 ms. The automatic gain control target was set to $3 \times 10^6$ (full scan) and $5 \times 10^5$ (dd-MS/MS). Heated electrospray ionization (HESI) parameters included sheath gas flow rate of 50 arb, auxiliary gas flow rate of 10 arb, sweep gas flow rate of 2 arb, spray voltage of 3 kV, and capillary temperature of 320 °C. Data processing was performed using the Xcalibur 4.1 (Thermo Fisher Scientific) software system. MS detection was performed in the positive polarity mode, and the method running time was 30.01 min.

### 2.3. Enzymatic activity and inhibition assays

A Förster resonance energy transfer (FRET)-based enzymatic assay was used to discover SARS-CoV-2 $M^{pro}$ inhibitors, which were used to screen peptides Ac-Tβ4 and its metabolites to identify potential inhibitory compounds. The fluorescently labeled substrate, DABCYL-KTSAVLQSGFRKME-↓EDANS, used in the enzyme inhibition assay was procured from BPS Bioscience. The fluorescence of the substrate was quenched using the dabcyl dye at a normal state. Upon digestion by the enzyme, the substrate exhibited a 5-((2-Aminoethyl)amino)naphthalene-1-sulfonic acid (EDANS) segment-generated fluorescence signal. All the peptides were prepared in 0.1 % acetic acid at a stock concentration of 10 mM. In the $M^{pro}$ enzyme inhibition experiment, 370 nM of in-house-prepared SARS-CoV-2 $M^{pro}$ and 10 μM of each chemical were combined in a reaction buffer (20 mM Tris-Cl, pH 7.4) in a 96-well plate. The reaction proceeded by dispensing 20 μM FRET substrate.

Fluorescence readings were recorded every 1 min for 30 min following reaction initiation using a Synergy multi-plate reader (BioTek) at 360 nm excitation and 460 nm emission wavelengths. A negative control (enzyme and substrate) and several positive controls (enzyme, substrate, GC 376, Boceprevir, and baicalein) were used to assess the experimental approach. Six distinct inhibitor concentrations (100 μM–97.65 nM) were selected to calculate the half-maximal inhibitory concentration ($IC_{50}$) value.

### 2.4. Cloning, protein expression, and purification of $M^{pro}$

The SARS-CoV-2 $M^{pro}$ gene derived from the Wuhan-Hu-1 isolate was obtained from Integrated DNA Technologies (https://sg.idtdna.com/). pET21a (+) plasmids containing the SARS-CoV-2 $M^{pro}$ sequence were introduced into competent *Escherichai coli* BL21 (DE3) cells. A single colony was selected to initiate a 4 mL liquid culture supplemented with 0.1 mg/mL ampicillin, which was incubated overnight in a shaking incubator (37 °C, 180 rpm). This inoculum was subsequently transferred (1:100 ratio) to a 400 mL liquid culture supplemented with 0.1 mg/mL ampicillin, grown to an optical density (OD) value of 0.4–0.5 at 600 nm, and induced with 0.5 mM isopropyl β-D-1-thiogalactopyranoside (IPTG). Post-induction, the cultures were incubated for 3 h (37 °C, 180 rpm) and harvested (30 min, 4000 rpm, 4 °C). The harvested culture was resuspended in a BugBuster Master Mix reagent and processed following the manufacturer's protocol. Cell debris was removed through centrifugation (14,000 rpm, 10 min, 4 °C), and the resulting supernatant was incubated with nickel-nitrilotriacetic acid (Ni-NTA) beads (1 h, 4 °C) on a rotator. The beads were thoroughly washed with buffer A (50 mM Tris-HCl, pH 8.0, 300 mM NaCl, 1 mM dithiothreitol [DTT], and 20 mM imidazole) and eluted with buffer B (50 mM Tris-Cl, pH 8.0, 300 mM NaCl, 1 mM DTT, 300 mM imidazole, and 10 % glycerol). The eluted protein was concentrated using a 10,000 molecular weight cutoff (MWCO) centrifugal concentrator spin column. Subsequently, desalting was performed using fast protein liquid chromatography (FPLC) to ensure protein purity, which was confirmed using sodium dodecyl sulfate-polyacrylamide gel electrophoresis (SDS-PAGE). Protein concentration was determined by measuring the absorbance at 280 nm using a NanoDrop 1000 Spectrophotometer V3.8.

### 2.5. Isothermal titration calorimetry (ITC) measurements

The thermodynamic characteristics of the binding interaction between $M^{pro}$ and the peptides Ac-T$\beta_{1\text{-}14}$ and Ac-T$\beta_{1\text{-}17}$ were assessed using ITC. ITC experiments were conducted using a MicroCal PEAQ-ITC instrument (Malvern Panalytical, Malvern, UK) at 25 °C. The peptides were dissolved in 0.1 % acetic acid and diluted with protein elution buffer, and the protein buffer was adjusted using acetic acid to ensure buffer homogeneity. The $M^{pro}$ concentration was determined based on its absorbance at 562 nm, using the BCA assay. During the experiment, 60 μL of each compound was loaded into a syringe and titrated with 300 μL of $M^{pro}$ protein within the ITC cell. The injections consisted of an initial 0.4 μL followed by 19 identical injections of 2 μL, each lasting 4 s, with 120 s intervals between injections. The stirring speed was set to 750 rpm, and the reference power was maintained at 10 μcal/s with the reference ampoule containing ultrapure water. All solutions were degassed and filtered through a 0.2 μm membrane filter. Control experiments involved injecting the ligand solution into the buffer and the buffer into the $M^{pro}$ protein solution using an identical protocol. The cell and syringe concentrations were 30 μM and 3 mM, respectively, ensuring adherence to an acceptable c-value range. Enthalpy change (ΔH), free energy change (ΔG), entropy change (ΔS), dissociation constant ($K_d$), and reaction stoichiometry (n) were determined using Microcal PEAQ-ITC analysis software, with each measurement performed twice. The data were fitted to a one-site binding model. Binding constants within the acceptable range were assessed based on c values between 1 and 1000, calculated using the following formula:

$$c = nK_a[M]T = n[M]T/K_d$$

(where n represents the stoichiometry of interaction, $K_a$ represents the binding constant, [M] represents the total macromolecular concentration, and T represents the absolute temperature).

The Gibbs energy and change in entropy were computed using the following formulas:

$$\Delta G = -RT \ln K_b$$

(where R represents the gas constant, T represents the absolute temperature, and $K_b$ represents the binding constant), and $\Delta G = \Delta H - T\Delta S$.

### 2.6. Cytotoxicity assay

A cytotoxicity assay was performed in NIH/3T3 and HUVECs following a 24-h growth in a 96-well plate, with 10,000 cells per well. The control group was treated with media only, and the peptide-treated groups were exposed to peptide-supplemented media for incubation. In all the treatments, peptide concentration was 6.25–50 μg/mL. The cells were allowed to grow cultured for 24 h at 37 °C and 5 % $CO_2$. After 24 h, the wells were treated with 10 μL of cell counting kit-8 solution (CCK-8; Dojindo Laboratories, Kumamoto, Japan). Subsequently, the plates were incubated at 37 °C for 1 h, and the absorbance was measured at 450 nm using a microplate reader (GloMax Discover System, Promega, USA). The OD values were used to calculate cytotoxicity.

### 2.7. Hemolysis assay

The peptide fragments were assessed for hemolysis by exposing them to rat blood samples [31,32], using a specifically formulated glycine-buffered saline to stabilize red cells (ID-CellStab; Bio-Rad, Switzerland). Red blood cells (RBCs) (200 μL, $10^5$ cells) were exposed to various peptide concentrations (62.5, 125, 250, 500, and 1000 μg/mL). As a positive control, 10 μL of 2 % SDS solution was added to the blood (0.1 % SDS final volume). The solutions were maintained in a water bath at 37 °C for 30 min and subsequently centrifuged. The supernatant was analyzed using an ultraviolet (UV)–visible spectrophotometer at a wavelength of 540 nm. The negative control contained RBCs and 0.05 % SDS solution in distilled water (DW).

### 2.8. Wound healing assay

A wound healing assay was performed on fully confluent HUVECs in a single layer in a 12-well plate. Uniform wounds were created across the confluent cell monolayer using a sterilized 200 μL pipette tip. Cell debris was removed by repeated washing with 1 × phosphate-buffered saline (PBS), and peptide-treated (25 μg/mL) medium was added for incubation. The cells were allowed to migrate into the wound area for 8 h at 37 °C, and digital photos were captured at 0 and 8 h using a bright field microscope. The wound area (within each plate) was calculated using the ImageJ software (National Institutes of Health, Bethesda, MD, USA). The percentage of wound closure was quantified by subtracting the healed wound area at 8 h from the initial wound area. Each experiment was performed thrice using triplicate wells.

### 2.9. Tube formation assay and ROS generation

For the tube formation assay, confluent HUVECs were harvested and seeded in a pre-coated slide chamber (8-well cell culture slides; SPL, South Korea) with a basement membrane matrix (Geltrex™, Thermo Fisher Scientific, South Korea) at a density of $1 \times 10^4$ cells per chamber. The ROS groups were treated with 10 μL $H_2O_2$ (200 μM) to generate ROS. The parent and peptide metabolite concentrations in the medium were both 25 μg/mL. Following a 24-h incubation, tubular networks were observed using a bright field microscope. The tube formation

parameters were analyzed using ImageJ software (NIH, USA).

### 2.10. Preparation of peptide scaffold

The scaffold was prepared by initially mixing 1.25 % Gelzan in 8 ml DW. The solution was heated and stirred at 70–80 °C and 300 rpm for 30 min. Subsequently, 2 ml 0.18 % $CaCl_2$ was added as a crosslinker, and the stirring speed was increased to 700 rpm. Further, 0.2 % Ac-T$\beta_{1\text{-}17}$ (20 mg/10 mL) peptide was added to the mixture and stirred for 10 min. The solution was ultrasonicated for 30 s and pipetted into 4-well plates. The wells were frozen at −70 °C for 4–6 h. Finally, the scaffold was freeze-dried for 24 h.

### 2.11. Characterization of peptide scaffold

The surfaces and cross sections of the samples were examined using a scanning electron microscope (SEM) (Inspect50, FEI, USA) to assess surface properties. Before imaging, samples were coated with sputtering of platinum ions (E−1045, Hitachi, Japan) to enhance conductivity and contrast. Energy-dispersive X-ray spectroscopy (EDS) integrated with SEM was employed to analyze the distribution and composition of elements. Sample surface modification was analyzed using the Fourier transform infrared (FT-IR) spectroscopy with attenuated total reflectance (ATR) mode. Ac-T$\beta_{1\text{-}17}$ scaffolds were immersed in PBS at 2 g/10 mL and incubated at 37 °C in an incubator for qualitative and time-kinetic quantification. The resulting extracts were filtered using Millipore filters (0.22 μm) for sterilization. UV spectrophotometer (GENESYS, Thermo Fisher Scientific Korea Ltd, South Korea) at 230 nm was used to measure peptide concentration, and the standard peptide was used for creating a calibration.

### 2.12. Preparation of scaffold extract

Extracts were prepared using the following methods to assess the biocompatibility of scaffolds. The control and Ac-T$\beta_{1\text{-}17}$ scaffolds were immersed in HUVEC culture medium at a concentration of 2 g/10 mL and shaken at 37 °C in an incubator for 24 h. The resulting extracts were filtered using Millipore filters (0.22 μm) for sterilization.

### 2.13. In vitro biocompatibility assay using scaffold extracts

The Ac-T$\beta_{1\text{-}17}$ scaffold extracts were subjected to a crucial in vitro biocompatibility assay. The extracts were diluted to a specific concentration in the culture medium for the cytotoxicity assay using the CCK-8 (Dojindo, Japan). HUVECs were cultured at the desired passage, and the cells were seeded in 96-well plates at a density of $5 \times 10^3$ cells per well. Following a 24-h incubation, the medium was replaced with Ac-T$\beta_{1\text{-}17}$ hydrogel extract and further incubated for 24 h. Finally, 10 μL of the CCK-8 solution was added to each well and incubated for 1 h. Absorbance was measured at 450 nm using a microplate reader (BioTek, USA).

### 2.14. Cell proliferation on peptide scaffold

HUVECs were cultured on a scaffold substrate for 24 h. Each well of a 4-well plate was inoculated with a cell suspension of 50,000 cells. The control group comprised of scaffolds without peptides, whereas the test group comprised of peptide scaffolds. The cells were cultured for 24 h in an incubator at 37 °C and 5 % $CO_2$. After 24 h, the media were collected, and scaffolds were stained using a live-dead staining kit (Biotium, Inc., CA, USA). Finally, the samples were visualized and photographed using a fluorescence microscope (ZEISS Axio Imager 2).

### 2.15. Tube formation assay on peptide scaffold

HUVECs were cultured on a scaffold pre-coated with a basement membrane matrix (Geltrex™). A cell suspension of 50,000 cells was added to each well of a 4-well plate. The control group used a scaffold without peptides, whereas the test group used a peptide scaffold. The cells were cultured for 24 h at 37 °C and 5 % $CO_2$. After 24 h, the media were collected, and the scaffolds were stained with a live-dead staining kit (Biotium, Inc., CA, USA). Finally, microscopic images were captured by a fluorescence microscope (ZEISS Axio Imager 2).

### 2.16. Proteomics study of peptide-treated HUVECs

HUVECs were cultured with or without the Ac-T$\beta_{1\text{-}17}$ peptide. After aspirating the media and washing with PBS, 1 mL of lysis buffer (Pierce radio-immunoprecipitation assay [RIPA] buffer and Halt Protease Inhibitor Cocktail) was added. The cells were collected in a microfuge tube using a cell scraper and were sonicated twice for 30 s ON and 30 s OFF, centrifuged (20,000×*g*, 30 min, 4 °C), and the supernatant was collected. Protein concentrations were measured and normalized to prepare the samples. All samples were reduced with 100 mM DTT in 50 mM ammonium bicarbonate (ABC) to a final concentration of 10 mM DTT and incubated at 56 °C for 40 min. A 100 mM iodoacetamide (IAA) was added to a 50 mM ABC solution to alkalize the samples and achieve a final concentration of 20 mM IAA. The samples were incubated for 30 min at room temperature in the dark. Subsequently, the samples were reduced using 100 mM DTT in a 50 mM ABC solution to achieve a final concentration of 10 mM DTT and incubated for 10 min at room temperature in the dark. Trypsin was subsequently added to the protein samples at a ratio of 1:30 and lysed for 24 h at 37 °C. The following day, the second trypsin digestion was performed at a ratio of 1:100 in 80 % ACN for 2 h at 37 °C. The samples were subsequently spun down, and digestion was stopped using 5 % FA. The samples were dried in a speed vac at 60 °C until thoroughly dried. Subsequently, the samples were cleaned using an oasis hydrophilic-lipophilic balance-solid phase extraction (HLB-SPE) column, activated using methanol and ACN, and equilibrated using 0.1 % FA. The samples were loaded and rewashed using 0.1 % FA and eluted using 40, 60, and 80 % ACN. Finally, the samples were dried in a speed vac at 60 °C until thoroughly dried. Finally, the samples were resolubilized using 0.1 % FA, and 10 μL was injected into the LC-MS/MS system.

Data were collected using a Shimadzu liquid chromatography instrument and Q-Exactive MS/MS device. The separation process was performed using an ACE C18 column (100 × 2.1 mm, 5 μm; Advanced Chromatography Technologies, Aberdeen, UK) at 35 °C. Samples were eluted using a 40-min method starting with a gradient from 2 to 45 % methanol containing 0.1 % FA (Phase B), reaching 95 % over the subsequent 5 min, 2 % in the last 5 min. Full-scan MS spectra were obtained in the 200–2000 *m/z* range at a resolution of 70,000. The resulting MS/MS data were analyzed using Proteome Discoverer software (v.2.4) label-free quantitative proteomics [33], with precursor and fragment mass tolerances set to 10 ppm and 0.02 Da, respectively. To ensure accuracy, the maximum peptide and site false discovery rates were specified at 0.01 using Percolator. Subsequently, data were analyzed using the MetaboAnalyst platform (www.metaboanalyst.ca) for multivariate analysis [34]. Volcano plots were generated based on a fold change of 1.5; p-values <0.05 were considered to draw volcano plots. SRplot queried enhanced biological processes, and Gene Ontology (GO) enrichment analysis was performed using upregulated genes with p-values <0.05 and >1.5 fold changes [35].

### 2.17. Gene expression using RT-PCR

For gene expression analysis, quantitative real-time reverse transcription polymerase chain reaction (RT-PCR) was performed on mRNA samples obtained from HUVECs, untreated or treated with the Ac-T$\beta_{1\text{-}17}$ peptide. TRIzol reagent (Invitrogen, USA) was used to extract total mRNA from cell samples. The mRNA samples were purified using a QIAGEN RNeasy Mini Kit, following the manufacturer's protocol (QIAGEN, USA). The RNA quality (260/280 ratio) and concentration were

measured using a UV photometer (Eppendorf, Germany). The mRNAs were reverse-transcribed into cDNA using a reverse transcriptase kit (Takara Bio, South Korea). The real-time RT-PCR was performed using a commercial SYBR Green Supermix kit. The housekeeping gene glyceraldehyde-3-phosphate dehydrogenase (GAPDH) was used as an endogenous control whose primer efficiency was similar to the target genes. Each gene was normalized to GAPDH for all samples. Relative gene expression was expressed as the fold-change in mRNA/GAPDH abundance compared to the corresponding reference control. The forward (Fp) and reverse primer (Rp) sequences are listed in Supplementary Table 2.

### 2.18. Molecular docking

Molecular docking was performed on the energy-minimized model structure of the SARS-CoV-2 $M^{pro}$ protein (PDB ID: 7WO3) [36]. All the peptides under assessment were docked into the protein's active site, using Auto Dock Vina to prepare all the structures, small molecules, and proteins [37]. Similar tools were used to determine the protonation, protomer, tautomer, and ionization states. Using the Bond Order method, the Gasteiger charge of the protein was calculated as −4.012. The same method was used for small-molecule preparations to determine the number of rotatable bonds. Molecular docking between the protein and each small molecule was performed using Auto Dock 4.2 using the Lamarckian algorithm inside a 20 × 20 × 20 Å 3 grid box at X = 19.418335, Y = 13.416064, and Z = 26.710663 coordinates with an exhaustiveness of 12. Docking images were drawn using the BIOVIA Discovery Studio Visualizer (www.3ds.com/products/biovia).

### 2.19. Fetal mouse metatarsal angiogenesis assay

We extracted the metatarsal bones from C57BL/6 mouse embryos at E16.5 and carefully removed the skin, leaving intact tarsal and metatarsal bones. The institutional animal ethics committee of the Korea Institute of Science and Technology (KIST) approved experimental procedures for animal study (KIST-IACUC-2025-001). Only the middle three metatarsals were used in the experiment. These metatarsals were cultured in 4-well glass slide plates coated with a basement membrane matrix (Geltrex™) and gelatin for 24 h. Subsequently, the cells were treated with 25 μg/mL of Ac-$Tβ_{1-17}$ for 5 days. Following treatment, the samples were fixed and stained with fluorescein isothiocyanate (FITC)-conjugated CD31 antibody. VECTASHIELD® antifade mounting medium with DAPI was used to mount the glass slides onto the 24-well plates (Vector Laboratories, USA). Images were captured using a confocal laser scanning microscope (Carl Zeiss, Oberkochen, Germany) and analyzed using the Wimasis angiogenesis analysis platform. (Wimasis, www.wimasis.com).

### 2.20. Statistical analysis

The data were expressed as mean ± standard error of the mean (SEM). An unpaired two-tailed Student's t-test was performed to analyze the differences between the two groups and a one-way analysis of variance (ANOVA) was used to compare multiple groups using GraphPad Software (GraphPad Software, Inc., California, USA). Additionally, we used a two-way ANOVA to compare the groups in the time-kinetic experiments. A p-value is considered statistically significant between different groups for all tests (*$p < 0.05$, **$p < 0.01$, ***$p < 0.001$).

## 3. Results and discussion

The study of metabolites obtained from novel compounds and drugs, highlighting their functional mechanisms and effects, is a common research theme [38]. However, the metabolic processes of natural proteins remain largely unexplored. Research on the metabolism of peptide hormones, growth factors, related substances, and mimetics remains relatively limited [39], likely because of their rapid breakdown in the stomach, which hinders their progression to classical liver metabolism [40]. Despite this challenge, natural source-derived small peptides have numerous biological functions [41,42]. Assessing the biological functions of these peptides can result in the identification of novel functional peptide fragments and offer insights into their therapeutic potential and mechanisms of action (Fig. 1). In this study, we selected Ac-Tβ4 protein metabolites to assess the therapeutic potential in biomaterials.

### 3.1. Selection of potent peptide metabolites with antiviral activity

Ac-Tβ4 has one of the most fragmented protein sequences. Over the past 40 years, researchers have hypothesized and assessed numerous Ac-Tβ4 fragments for their biological activities (Supplementary Table 1). These fragments are known to increase cell proliferation [21], wound healing [22], and cellular migration [4]. Interestingly, all the previously reported fragments were either the active sites of the protein or randomly produced sequences from Ac-Tβ4. For the first time, we identified and reported 13 novel Ac-Tβ4 metabolites in both in vitro and in vivo experiments [28,29]. Ten peptides were synthesized for identification, with a purity of 95∼99 % (Table 1, Supplementary Fig. 1). Six of these have been identified as natural Ac-Tβ4 metabolites produced in biological samples, and are considered safe due to the biological compatibility of Ac-Tβ4 [43]. We aimed to understand the biological activities of the metabolite of Ac-Tβ4. Because these sequences are generated from their parent molecules, these peptides have the potential to become potent drugs or materials. However, testing each peptide individually is time-consuming and rigorous. Therefore, in this study, a screening method was used to identify a peptide metabolite that is more potent than the parent protein. Ac-Tβ4 and 10 fragment peptides produced from Ac-Tβ4 were commercially synthesized and screened using FRET-based SARS-CoV-2 $M^{pro}$ inhibition assay [44,45].

### 3.2. FRET-based screening against $M^{pro}$

Initially, six Ac-Tβ4 metabolites, four artificial fragments, and four positive controls (not shown in Table 1) were screened at 100 μM (Table 1). Ac-$Tβ_{1-14}$ and Ac-$Tβ_{1-17}$ exhibited >80 % inhibition of $M^{pro}$, which is a significant result compared to Ac-Tβ4 with only 7.09 % inhibition (Table 1). Peptides exhibiting >50 % inhibition during primary screening and their parents were selected for $IC_{50}$ studies. $IC_{50}$ assessments were conducted for the parent Ac-Tβ4 and two metabolites (Ac-$Tβ_{1-14}$ and Ac-$Tβ_{1-17}$). Both peptides ($IC_{50}$ values of 26.1 and 22.4 μM for Ac-$Tβ_{1-14}$ and Ac-$Tβ_{1-17}$, respectively) demonstrated inhibition for SARS-CoV-2 $M^{pro}$ (Fig. 2B & C). However, no inhibition was observed for the parent molecule Ac-Tβ4 (Fig. 2A).

The inhibitory activities of the peptide metabolites were associated with their amino acid sequences, indicating that the presence or absence of the C-terminal amino acid sequence may affect their activity levels (Fig. 2D). To understand this phenomenon, hypothesized in silico fragments were docked with the SARS-CoV-2 $M^{pro}$ protein (PDB ID: 7WO3). We observed that both the N-terminal fragment (Ac-SDKP, −7.3 kcal) and the C-terminal fragment (EKFDKS, −7.1 kcal) exhibited the highest binding affinities to the $M^{pro}$ in silico (Supplementary Table 3), meaning that both termini have the potential to bind to $M^{pro}$. To prove, iterative peptide fragments were synthesized from the N- and C-terminals of Ac-$Tβ_{1-17}$ (Supplementary Table 4), then analyzed using the $M^{pro}$ inhibition assay (Fig. 2E). However, among the 30 synthesized peptides, only the C-terminal fragments FDKS and SKL demonstrated notable inhibition, with FDKS exhibiting an $IC_{50}$ of 63.16 μM (Fig. 2F–H). Even the N-terminal peptide fragments with high docking scores, Ac-SDKP and AC-SDKPDM, showed less than 50 % inhibition.

Despite high docking scores for the N-terminal fragment Ac-SDKP (−7.3 kcal) and C-terminal fragment EKFDKS (−7.1 kcal) peptides (Supplementary Table 3), the in vitro assay results revealed a difference. This finding underscores the significance of in vitro assays over in silico

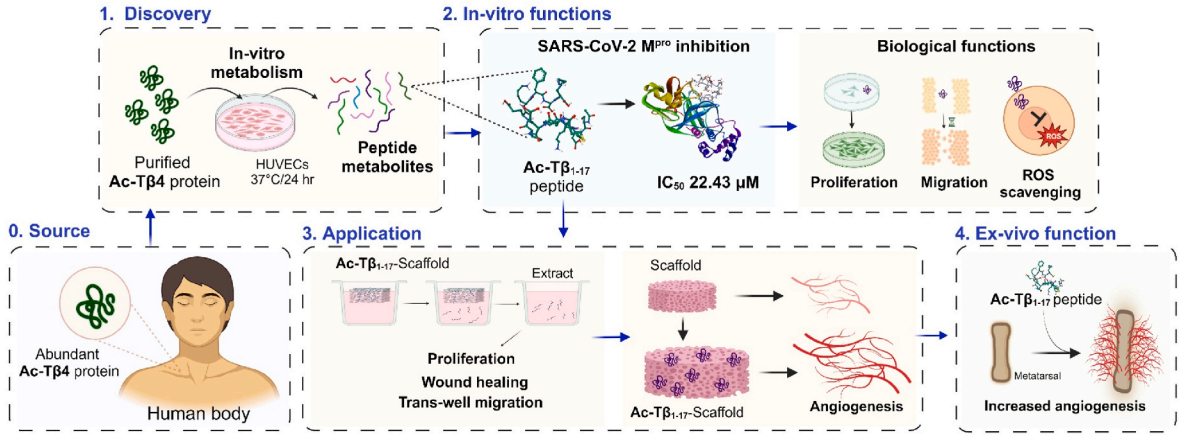


**Fig. 1.** Illustration of the use of protein-derived peptide metabolites for application in biomaterials. The human body produces the Ac-Tβ4 protein, which, when metabolized in vitro, produces the Ac-Tβ$_{1-17}$ peptide. This research demonstrated that Ac-Tβ$_{1-17}$ peptide, a metabolite of Ac-Tβ4 protein, exhibits amplified antiviral and proangiogenic activities compared to the parent Ac-Tβ4 protein and has implications in peptide-scaffold preparation.

**Table 1**
Synthesize peptide sequence of Ac-Tβ4 and its metabolites and their respective M$^{pro}$ inhibition activity.

| Synthesized Peptide Sequence | MW | Purity of STDs | Metabolism systems | | | | | | | | | Present study |
|---|---|---|---|---|---|---|---|---|---|---|---|---|
| | | | CPB[b] | LAP[c] | Trypsin /EDTA | rhAPN[e] | rhCPB1[d] | rhCPM[f] | LAP | HKM[g] | HUVEC | Rats | M$^{pro}$ inhibition (%) |
| Ac-Tβ4 | 4960.48 | 99.00 % | Parent protein | | | | | | | | | | **7.09** |
| Ac-Tβ4$_{31-43}$ | 1476.57 | 96.55 % | D[a] | – | – | – | – | – | D | – | D | – | **1.88** |
| Ac-Tβ4$_{1-11}$ | 1304.45 | 96.27 % | – | D | – | – | – | – | D | – | D | – | **1.25** |
| Ac-Tβ4$_{17-43}$ | 3071.41 | 95.86 % | D | – | – | D | D | – | – | D | D | – | **25.16** |
| **Ac-Tβ4$_{1-14}$** | 1694.89 | 97.46 % | – | D | – | – | – | – | D | D | D | D | **81.55** |
| Ac-Tβ4$_{1-15}$ | 1781.97 | 96.93 % | – | – | – | D | D | D | D | – | D | – | **34.4** |
| **Ac-Tβ4$_{1-17}$** | 2023.31 | 96.19 % | – | – | – | D | D | D | D | – | D | – | **85.77** |
| Ac-Tβ4$_{1-23}$ | 2739.06 | 99.60 % | Artificial fragment of Ac-Tβ4$_{1-43}$ but not a metabolite | | | | | | | | | | **27.13** |
| Ac-Tβ4$_{3-43}$ | 4719.34 | 99.14 % | Artificial fragment of Ac-Tβ4$_{1-43}$ but not a metabolite | | | | | | | | | | **35.09** |
| Ac-Tβ4$_{36-43}$ | 875.88 | 96.63 % | Artificial fragment of Ac-Tβ4$_{1-43}$ but not a metabolite | | | | | | | | | | **8.97** |
| Ac-Tβ4$_{1-3}$ | 390.39 | 99.19 % | Artificial fragment of Ac-Tβ4$_{1-43}$ but not a metabolite | | | | | | | | | | **9.27** |

MW, molecular weight.
**Data with "Bold" fonts indicate the metabolites included for M$^{pro}$ inhibition activity in this study. Ac-Tβ$_{1-14}$ and Ac-Tβ$_{1-17}$ peptides are the most active compared to other assay subjects.** The rest of the data are summarized from Rahaman et al., 2022 [28] and Rahaman et al., 2023 [29].
[a] D, detected as metabolite of Ac-Tβ4.
[b] CPB, porcine carboxypeptidase.
[c] LAP, porcine leucine aminopeptidase N.
[d] CPB1, recombinant human carboxypeptidase B.
[e] rhAPN, recombinant human aminopeptidase N.
[f] CPM, recombinant human carboxypeptidase M.
[g] HKM, human kidney microsomes; HUVEC, human umbilical vein endothelial cells.

screening. In silico screening, such as calculating the binding energy through docking, has limitations because it does not fully consider the natural conditions of peptide-protein binding. It often fails to orient ligands close to the experimental binding mode [46]. This research highlights the reliability and significance of in vitro assays in peptide-protein binding studies. The data from in vitro experiments, with their high reliability, surpassed those from in silico assessments. This confidence in our experimental process was reinforced by FDKS and SKL, which represent the C-terminal portion of Ac-Tβ$_{1-17}$. These results indicated the significance of the C-terminal domain in M$^{pro}$ inhibition. To test this hypothesis, we further assessed peptide-protein binding through isothermal calorimetry and in silico molecular docking studies. We aimed to illustrate the binding affinity and active-site interaction of Ac-Tβ$_{1-17}$ with M$^{pro}$ to further support our findings.

### *3.3. Assessment of thermodynamic parameters of M$^{pro}$-peptide binding using isothermal calorimetry (ITC)*

ITC is widely recognized for accurately estimating the binding affinities between compounds and proteins. It measures the heat changes during reactions, which can be either absorbed or released [46]. This method quantifies the thermodynamic parameters associated with molecular interactions (Fig. 3A). We determined the calorimetric dissociation constant ($K_d$) and complex stoichiometry (N) of Ac-Tβ$_{1-14}$-M$^{pro}$ and Ac-Tβ$_{1-17}$-M$^{pro}$ (Fig. 3B–E). The stoichiometry values, 1.05 and 0.87, indicated one peptide molecule binding to one M$^{pro}$ protein (Fig. 3F). The $K_d$ values of 19.4 μM and 22 μM, respectively, reflect moderate binding affinities. The negative binding energy (ΔG) (−6.43 and −6.87 kcal/mol) indicates spontaneous reaction processes and substantial binding affinities. Ac-Tβ$_{1-14}$ (ΔG of −6.43 kcal/mol) exhibits an enthalpy change (ΔH) and entropy change (-TΔS) of 40.3 and −46.73 kcal/mol, respectively, indicating endothermic and entropy-driven binding. In contrast, Ac-Tβ$_{1-17}$ (ΔG of −6.87 kcal/mol) exhibits an enthalpy change (ΔH) of −11.4 kcal/mol, reflecting exothermic binding, while its entropy change (-TΔS) of 4.53 kcal/mol contributes less significantly to the overall interaction. The stronger negative ΔG of Ac-Tβ$_{1-17}$ compared to Ac-Tβ$_{1-14}$, highlights its higher thermodynamic favorability against M$^{pro}$. These ITC data aligns with the

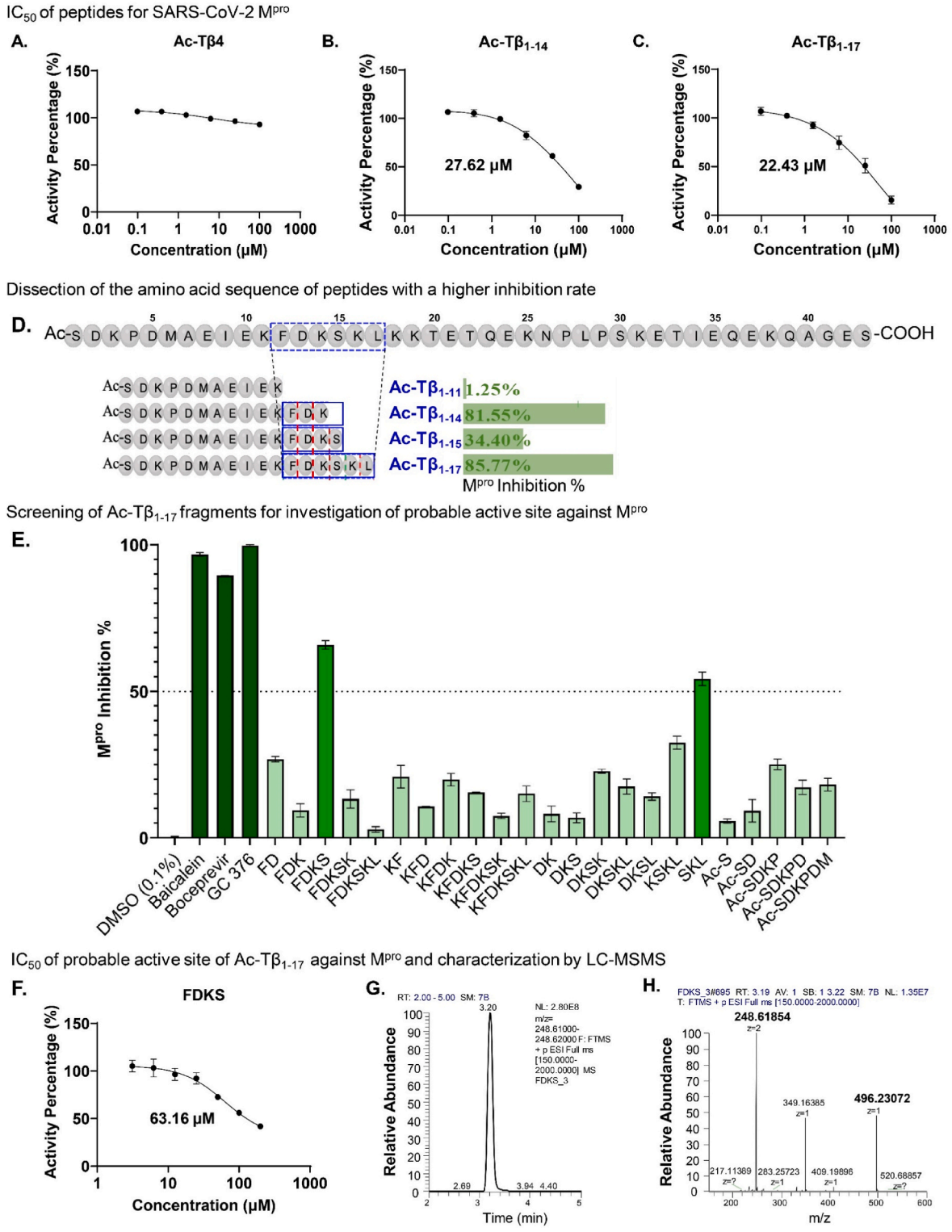


**Fig. 2.** Exploring the Ac-Tβ$_{1-17}$ sequence for identifying potential active sites targeting M$^{pro}$. The half-maximal inhibitory concentration (IC$_{50}$) of the parent protein and two metabolite peptides against SARS-CoV-2 M$^{pro}$ are determined (A–C). Dissection of the amino acid sequence of peptides in silico compared to the higher inhibition rate in vitro indicated the significance of the FDKSKL part (D). In vitro screening of Ac-Tβ$_{1-17}$ fragments to assess probable active sites against M$^{pro}$. FDKS and SKL exhibited >50 % inhibition activity (E). The IC$_{50}$ of FDKS peptide against SARS-CoV-2 M$^{pro}$ is assessed (F). The structure of the FDKS peptide is analyzed using liquid chromatography-tandem mass spectrometry (LC-MS/MS) (G & H).

FRET assay results, offering precise insights into the binding interactions between M$^{pro}$ protein and peptides. Therefore, we concluded that Ac-Tβ$_{1-17}$ was a more active peptide metabolite than that of Ac-Tβ$_{1-14}$.

Additionally, Ac-Tβ$_{1-17}$ fragment screening demonstrated that the C-terminal part of the peptide may have bonded to the active side of SARS-CoV-2 M$^{pro}$ and inhibited its activity (Fig. 2E). We conducted in silico docking to illustrate the binding between the peptide and M$^{pro}$ protein. Interestingly, the illustration of bonds between Ac-Tβ$_{1-17}$-M$^{pro}$ revealed

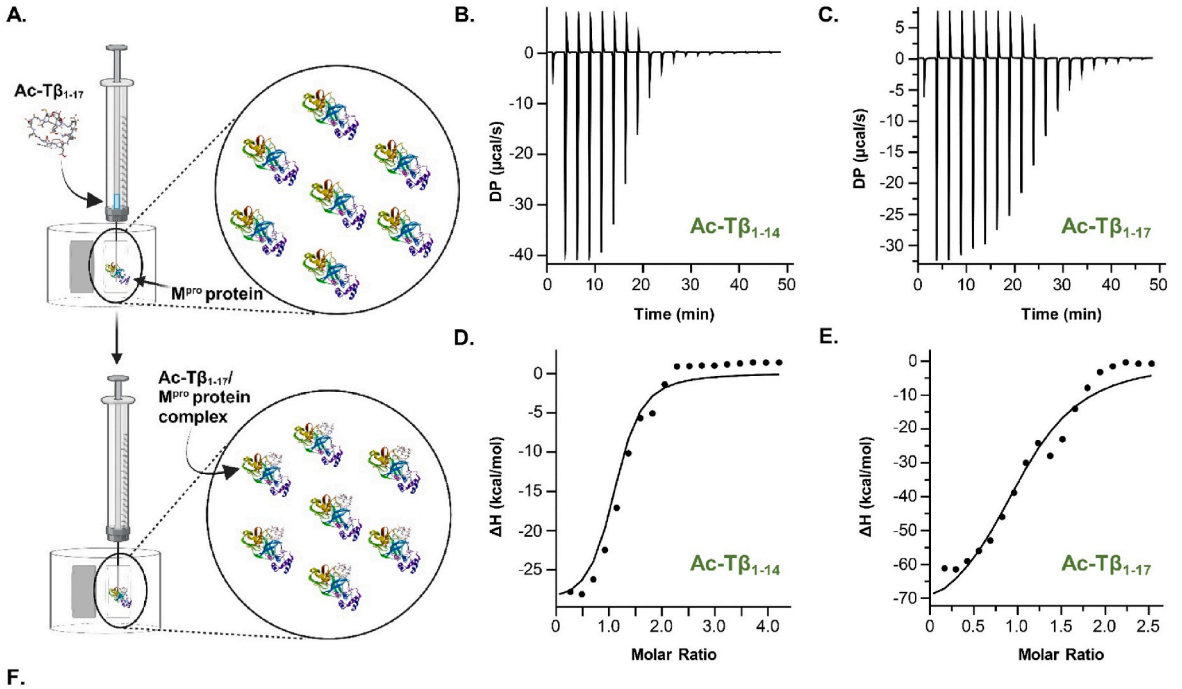


F.

| Protein Conc. | Inhibitor conc. | Dissociation Constant, $K_d$ (µM) | Stoichiometry (N) | Binding Energy, ΔG (kcal/mol) | Enthalpy Change, ΔH (kcal/mol) | Entropy Change, -TΔS (kcal/mol) |
|---|---|---|---|---|---|---|
| $M^{pro}$ (30 µM) | Ac-Tβ$_{1-14}$ (3 mM) | 19.4 ± 2.1 | 1.05 ± 0.13 | - 6.43 | 40.3 ± 2.50 | - 46.73 |
| | Ac-Tβ$_{1-17}$ (3 mM) | 22.0 ± 6.0 | 0.87 ± 0.15 | - 6.87 | - 11.4 ± 2.44 | 4.53 |

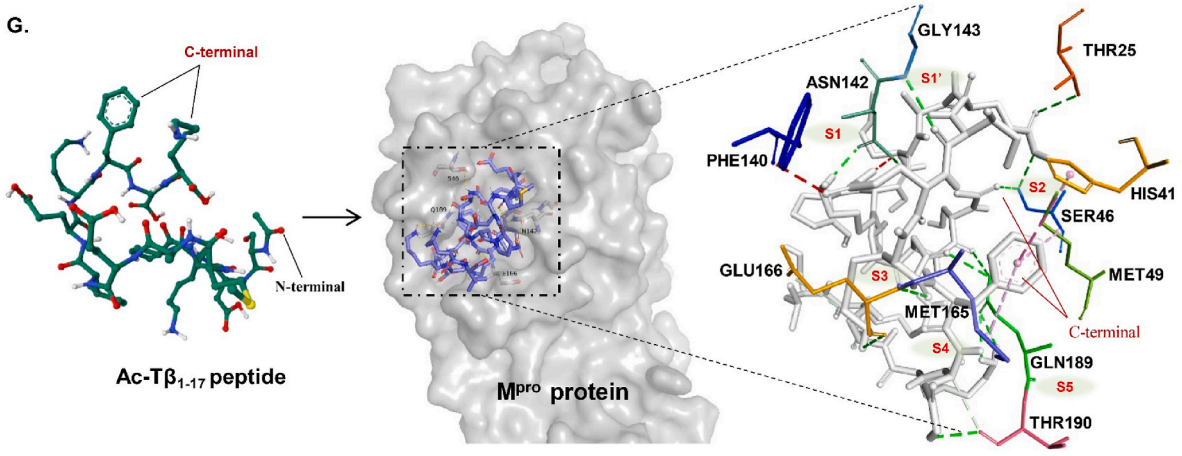


**Fig. 3.** Isothermal titration calorimetry (ITC) analysis and molecular docking of Ac-Tβ$_{1-14}$ and Ac-Tβ$_{1-17}$. Diagrammatic representation of the ITC process (A). Representative thermodynamic profiles of Ac-Tβ$_{1-14}$ and Ac-Tβ$_{1-17}$ binding with SARS-CoV-2 $M^{pro}$ in solution (B, C). The one-site theoretical binding model is fitted to the resulting data (D, E). Thermodynamic parameters of the interaction between peptides and $M^{pro}$ (F). Molecular docking results of Ac-Tβ$_{1-17}$ and $M^{pro}$. The dashed line indicates polar interactions between Ac-Tβ$_{1-17}$ and $M^{pro}$ (G).

that the C-terminal of Ac-Tβ$_{1-17}$ peptide binds (Binding affinity, −4.6 kcal/mol) with the $M^{pro}$ active site (x = 19.418335, y = 13.416064, and z = 26.710663) (Fig. 3G). Three hydrophobic bonds were observed between HIS41, MET49, and MET165, and Ac-Tβ$_{1-17}$ peptide. All three were associated with phenylalanine of Ac-Tβ$_{1-17}$ peptide at the S2 position of the SARS-CoV-2 $M^{pro}$ and Pi-Pi T-shaped, Pi-Alkyl bond, respectively (Fig. 3G and Supplementary Table 5). Additionally, hydrogen bonds were observed among SER46, THR25, GLY143, ASN142, PHE140, GLU166, GLU189, and THR190. A previous literature assessment revealed that our docking results and the position of the Ac-Tβ$_{1-17}$ peptide at the SARS-CoV-2 $M^{pro}$ binding site are valid [47]. Additionally, these data highlight the validity of our approach to assess peptide interactions at the active sites and represent a novel approach.

### 3.4. Cytotoxicity and hemolysis assessment of Ac-Tβ4 metabolites

Ac-Tβ4, Ac-Tβ$_{1-14}$, and Ac-Tβ$_{1-17}$ were assessed for cytotoxicity in NIH/3T3, HUVECs, and RBCs for hemolysis. Peptides are commonly infused intravenously (IV) or subcutaneously in animals to ensure rapid dispersion and prevent degradation [40]. However, the parent compound Ac-Tβ4 is safe for administration in various animal and human models [48]. This study aimed to compare the safety profiles of these metabolites. No cytotoxicity was observed in NIH/3T3 and HUVECs across the peptide dose ranges of 6.25–50 µg/mL (Fig. 4A and B). Cells

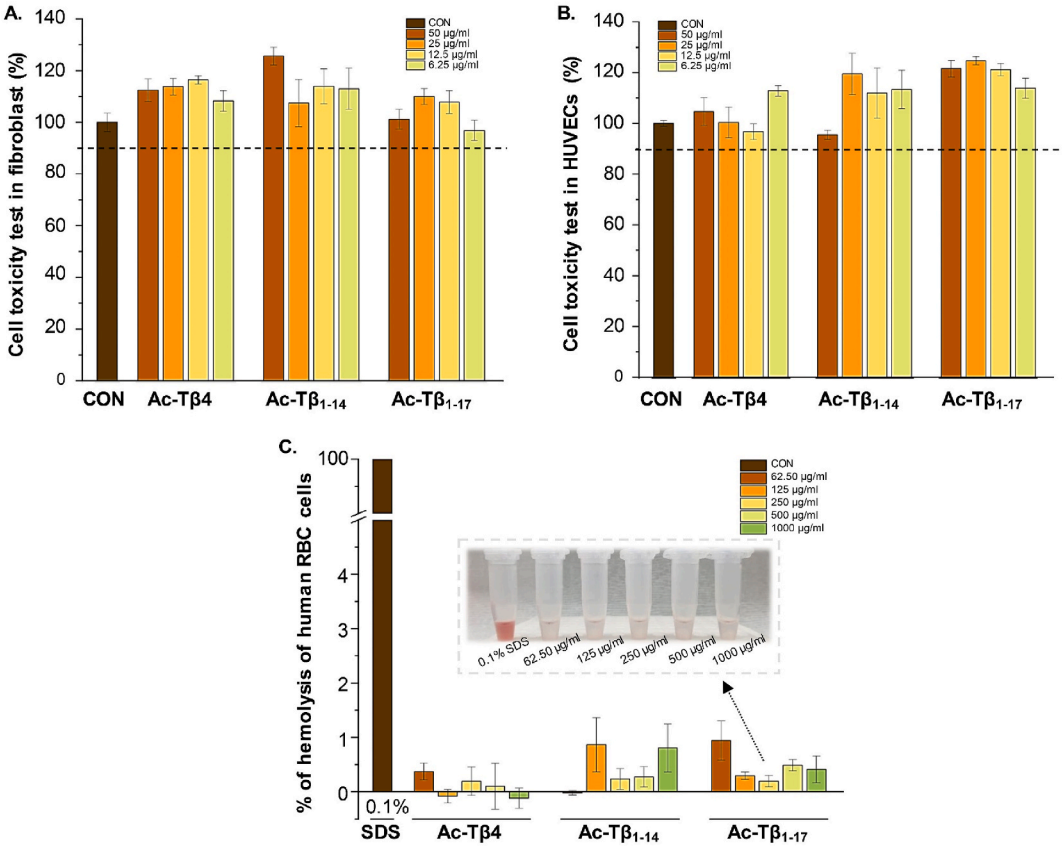


**Fig. 4.** Cytotoxicity screening of Ac-Tβ4 and its metabolites in fibroblasts (A), human umbilical vein endothelial cells (HUVECs) (B), and red blood cells (RBCs) (C). Treatment with Ac-Tβ4, Ac-Tβ$_{1\text{-}14}$, and Ac-Tβ$_{1\text{-}17}$ at various doses did not exhibit any toxicity with cell viability above 90 % dash line (A–B). Incubation of Ac-Tβ4 protein, Ac-Tβ$_{1\text{-}14}$, and Ac-Tβ$_{1\text{-}17}$ peptides with rat RBCs demonstrated no hemolytic activity (OD values < 1.5 % compared to 0.1 % sodium dodecyl sulfate [SDS]). Ac-Tβ$_{1\text{-}17}$ peptides with rat RBCs are illustrated in the inset compared to 0.1 % SDS (C). The data are presented as the mean ± SEM, with three samples per group.

treated with the control or peptide exhibited similar morphologies and health patterns. Additionally, the data demonstrated that Ac-Tβ4, Ac-Tβ$_{1\text{-}14}$, and Ac-Tβ$_{1\text{-}17}$ were safe to treat cells. 25 μg/mL dose of Ac-Tβ$_{1\text{-}17}$ produced the highest proliferation compared to other doses (Fig. 4B). Further experiments were conducted using 25 μg/mL peptide concentration.

In the RBC hemolysis assay, the peptide fragments were assessed by exposing them to rat RBC samples using five different concentrations (62.5, 125, 250, 500, and 1000 μg/mL). RBCs in RBC stabilizing buffer served as the standard control (0 % hemolysis), whereas SDS-treated (0.1 %) RBCs were considered as 100 % hemolysis and negative control. All peptides exhibited a hemolysis potential of <2 % compared to that of the standard control (Fig. 4C). We determined that the parent and its fragmented peptides were non-hemolytic at concentrations up to 1000 μg/mL. This study confirmed the safety of Ac-Tβ4 and its metabolites when administered intravenously or subcutaneously without causing RBC hemolysis.

### 3.5. *Wound healing and reactive oxygen species (ROS) scavenging activity of Ac-Tβ$_{1\text{-}17}$ in HUVECs*

Ac-Tβ4 enhances cell growth and wound healing by promoting cell proliferation and angiogenesis in HUVECs, a model widely used for angiogenesis studies [5,49]. This study aimed to compare the wound healing and cell proliferation activities of Ac-Tβ$_{1\text{-}17}$ with Ac-Tβ4. Cytotoxicity assays revealed that Ac-Tβ$_{1\text{-}17}$ promotes cell proliferation in HUVECs more effectively than Ac-Tβ4 (Fig. 4B). Furthermore, Ac-Tβ$_{1\text{-}17}$ exhibited inhibitory effect against SARS-CoV-2 M$^{pro}$, unlike Ac-Tβ4.

To assess wound-healing potential, HUVECs were treated with Ac-Tβ$_{1\text{-}17}$ or Ac-Tβ4 (25 μg/mL), and wound healing was evaluated by measuring the wound area at baseline (0 h) and after 8 h of incubation (Fig. 5A). Both peptides significantly enhanced wound closure compared to the control group, with Ac-Tβ$_{1\text{-}17}$ showing greater efficacy (Fig. 5B). These findings highlight the superior role of Ac-Tβ$_{1\text{-}17}$ in cell proliferation and wound healing compared to its parent protein, Ac-Tβ4.

Oxidative stress, caused by an imbalance between free radicals and antioxidants, can damage macromolecules like proteins and DNA [50]. ROS, such as hydrogen peroxide ($H_2O_2$), exacerbate oxidative stress and impair mitochondrial activity [51]. To assess ROS scavenging activity, we performed an assay using HUVECs exposed to $H_2O_2$, which disrupts tube formation, a marker of angiogenesis. Ac-Tβ$_{1\text{-}17}$ restored tube formation significantly(Fig. 5G), while Ac-Tβ4 failed to mitigate ROS-induced damage (Fig. 5C–F). Ac-Tβ$_{1\text{-}17}$ improved total tube length, branching length, and segment length (Fig. 5H–J), demonstrating its ROS-scavenging ability and potential to support angiogenesis by mitigating oxidative stress in HUVECs.

The remarkable functionality of Ac-Tβ$_{1\text{-}17}$ prompted further investigation of its incorporation into biomaterials [52]. This is particularly relevant as biomaterials often face extreme conditions during preparation, which can compromise the stability and functionality of growth factors, typically protein molecules [53]. Growth factors frequently encounter instability during preparation, limited lifespan after delivery, and rapid inactivation under physiological conditions [54].

### 3.6. *Characterization of peptide scaffold*

Ac-Tβ$_{1\text{-}17}$ scaffolds were prepared by incorporating gelatin, calcium chloride, and peptide molecules. Characterization included surface assessment and EDS mapping of nitrogen molecules. After scaffold preparation (Fig. 6A), the scaffolds were coated with platinum and

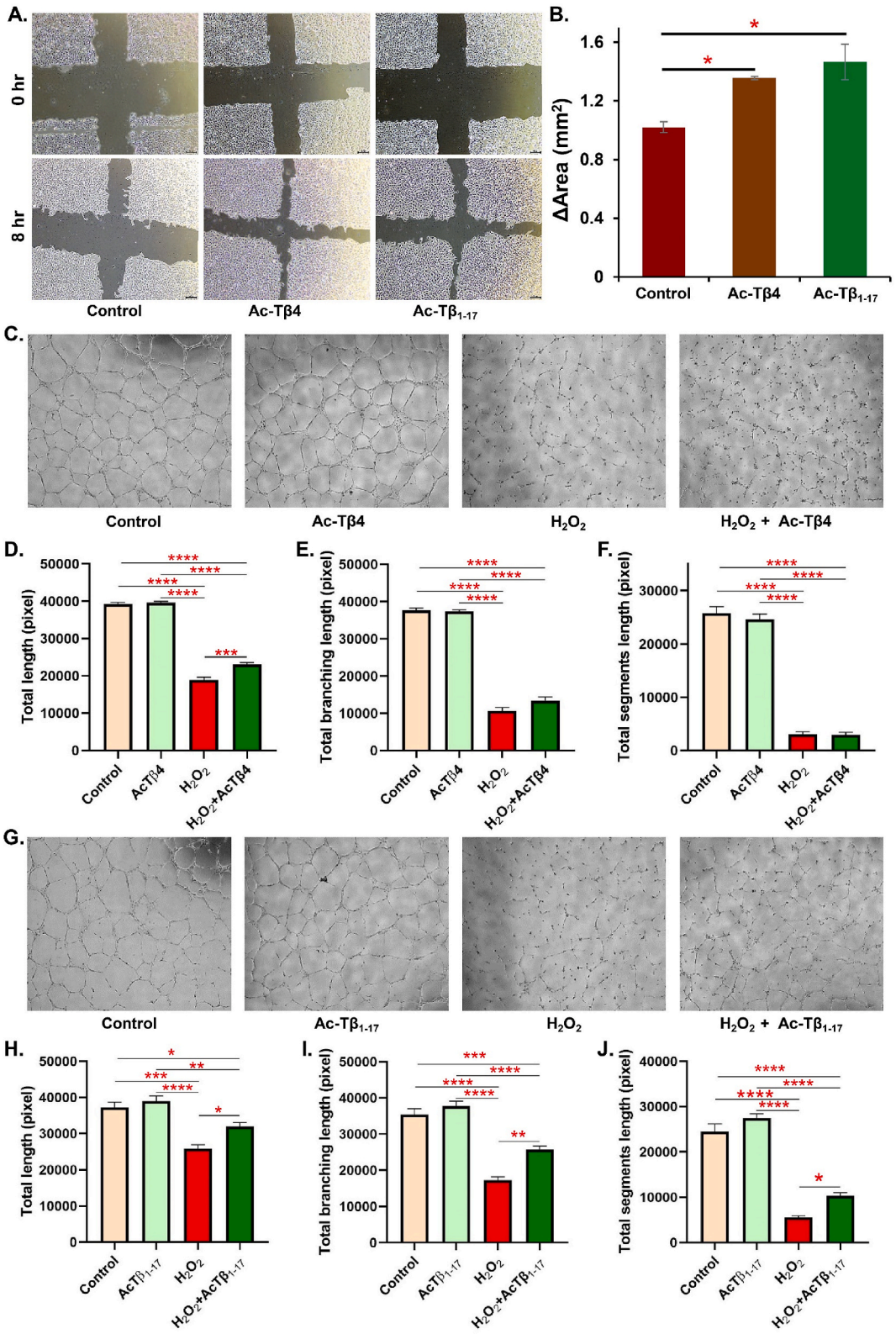


**Fig. 5.** Wound healing and reactive oxygen species (ROS) scavenging activity of Ac-T$\beta_{1\text{-}17}$ peptide. Microscopic images of wounds at 0 and 8 h post-treatment with 25 μg/mL of Ac-Tβ4 protein and Ac-T$\beta_{1\text{-}17}$ peptide (A). The wound healing activity is measured using ImageJ, and comparing the area covered by regular, 25 μg/mL dose of Ac-Tβ4 protein and Ac-T$\beta_{1\text{-}17}$ peptide. Asterisk (*) indicates significant differences compared with the control group (B). ROS inhibition by Ac-Tβ4 protein under simultaneous $H_2O_2$ treatment (C–F). ROS inhibition by Ac-T$\beta_{1\text{-}17}$ peptide under simultaneous $H_2O_2$ treatment (G–J). The data are presented as the mean ± SEM, with three samples per group. A p-value is considered statistically significant for all tests (ANOVA; *$p < 0.05$, **$p < 0.01$, ***$p < 0.001$, and ****$p < 0.0001$).

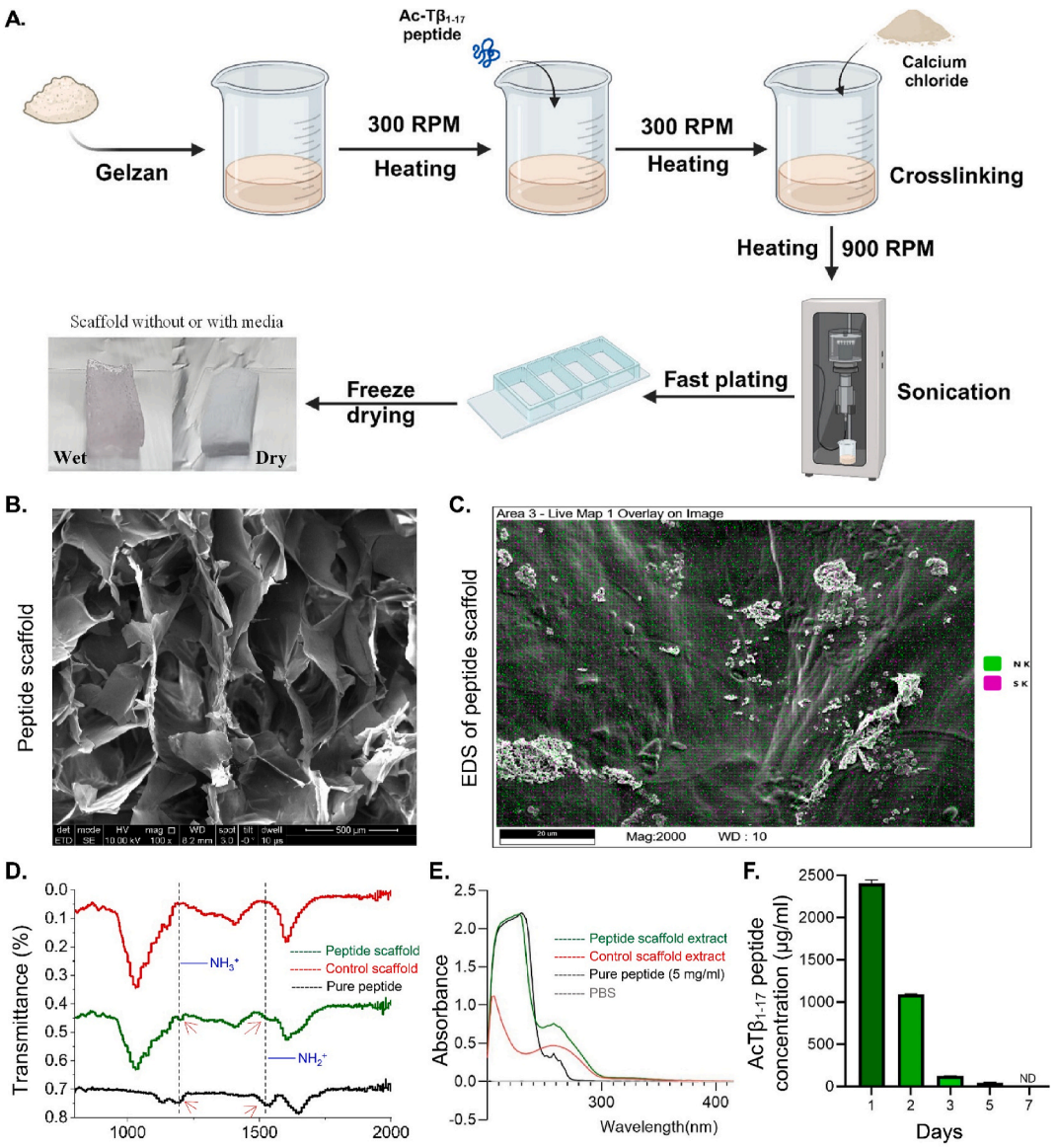


**Fig. 6.** Characterization of Ac-Tβ$_{1\text{-}17}$ scaffolds. Preparation of Ac-Tβ$_{1\text{-}17}$-integrated scaffold (A). Surface assessment of Ac-Tβ$_{1\text{-}17}$ scaffold using scanning electron microscopy (B). EDS characterization of Ac-Tβ$_{1\text{-}17}$ scaffold using SEM for nitrogen and sulfur integration on the scaffold surface (C). Transmittance (%) analysis of pure peptide, control, and Ac-Tβ$_{1\text{-}17}$ scaffolds using Fourier transform infrared (FTIR) spectroscopy. $NH_2^+$ and $NH_3^+$ generated peaks (red) from peptide (D). Extracts (100 %) from the control and Ac-Tβ$_{1\text{-}17}$ scaffolds are measured using an ultraviolet (UV) spectrophotometer at 230 nm and compared with the 5 mg/mL pure Ac-Tβ$_{1\text{-}17}$ peptide. The Ac-Tβ$_{1\text{-}17}$ scaffolds exhibited a peak similar to that of the pure peptide peak at a wavelength of 230 nm (E). The release of the Ac-Tβ$_{1\text{-}17}$ peptide from the scaffold was tracked over time at 1, 2, 3, 5, and 7 days (F).

analyzed using SEM, revealing a well-structured porous structure (Fig. 6B). EDS characterization further demonstrated the presence of nitrogen and sulfur molecules on the scaffold surface (Fig. 6C). The scaffolds were then powdered, dried, and analyzed using FT-IR spectroscopy for peptide-related peaks. The peptide IR spectra showed three distinct amide regions: amide I (centered at ~1650 cm−1), amide II (in the range of 1470–1570 cm–1), and amide III (in the range of 1250–1350 cm–1) [55]. Transmittance (%) analysis of pure peptide and Ac-Tβ$_{1\text{-}17}$ scaffolds showed that amide II ($NH_2^+$) and III ($NH_3^+$) from lysine produced distinct peaks for Ac-Tβ$_{1\text{-}17}$, reflecting the peptide's incorporation into the scaffold (Fig. 6D). In contrast, the control scaffold did not exhibit peaks in these regions, confirming that the observed peaks were specific to Ac-Tβ$_{1\text{-}17}$. This experiment confirmed that Ac-Tβ$_{1\text{-}17}$ was successfully incorporated into the scaffold and may contribute to cell proliferation and migration on or within the scaffold pores.

To assess peptide release, both scaffold groups were incubated in PBS for 24 h at 37 °C without stimulation. The PBS from the control scaffold, Ac-Tβ$_{1\text{-}17}$ scaffold, 5 mg/mL pure Ac-Tβ$_{1\text{-}17}$ solution, and PBS were measured using a UV spectrophotometer at 230 nm. Notably, both the Ac-Tβ$_{1\text{-}17}$ scaffold and 5 mg/mL pure Ac-Tβ$_{1\text{-}17}$ solution exhibited a similar peak corresponding to the Ac-Tβ$_{1\text{-}17}$ peptide. In contrast, the control scaffold showed a different pattern, indicating the absence of peptide (Fig. 6E). To assess the prolonged release of the peptide, time-dependent release of the Ac-Tβ$_{1\text{-}17}$ peptide from the scaffold at various time points (1, 2, 3, 5, and 7 days) were measured (Fig. 6F). A significant peptide release is observed within the first 24 h, with a high concentration peaking around day 1, followed by a noticeable decrease at day 2. From day 3 onwards, the peptide concentration remains extremely low, with negligible peptides detected by day 7. These data confirm that the peptide was incorporated into the scaffold and initial burst release of the peptide in the medium, followed by a slow depletion, with no detectable peptide remaining at day 6–7 at 37 °C.

### 3.7. Peptide scaffold extract increased proliferation and migration of HUVECs

The effect of Ac-Tβ$_{1-17}$ peptide released from the scaffold on HUVEC proliferation and migration was evaluated using cell proliferation, cytotoxicity, wound healing, and Transwell migration assays. Peptide release into the medium was observed after incubating the peptide-integrated scaffold for a specific time (Fig. 7A). The released peptide significantly increased HUVEC proliferation at 12 and 24 h compared to the control and normal scaffold groups (Fig. 7B). Cytotoxicity was assessed by measuring HUVEC viability after exposure to various scaffold extract concentrations (20–100 %) for 24 h (Fig. 7C). Results showed high biocompatibility, with cell viability remaining above 90 % at all concentrations. In a wound healing assay, 100 % Ac-Tβ$_{1-17}$ scaffold extract enhanced wound closure at 14, 16, 22, and 30 h compared to the control groups (Fig. 7D and E). Two-way ANOVA confirmed significant differences between the groups (n = 4) at these points. The Transwell migration assay, using calcein acetoxymethyl ester (AM) staining and fluorescence microscopy (Fig. 7F), demonstrated significantly increased migration in the presence of Ac-Tβ$_{1-17}$ scaffold extract (Fig. 7G).

These data show that Ac-Tβ$_{1-17}$, released by the scaffold, enhanced cellular biological functions in vitro and maintained scaffold biocompatibility. Notably, the scaffold preparation at high temperatures (80–90 °C) did not affect the biological effects, which is advantageous for peptides, as most growth factors are sensitive to temperature changes [56].

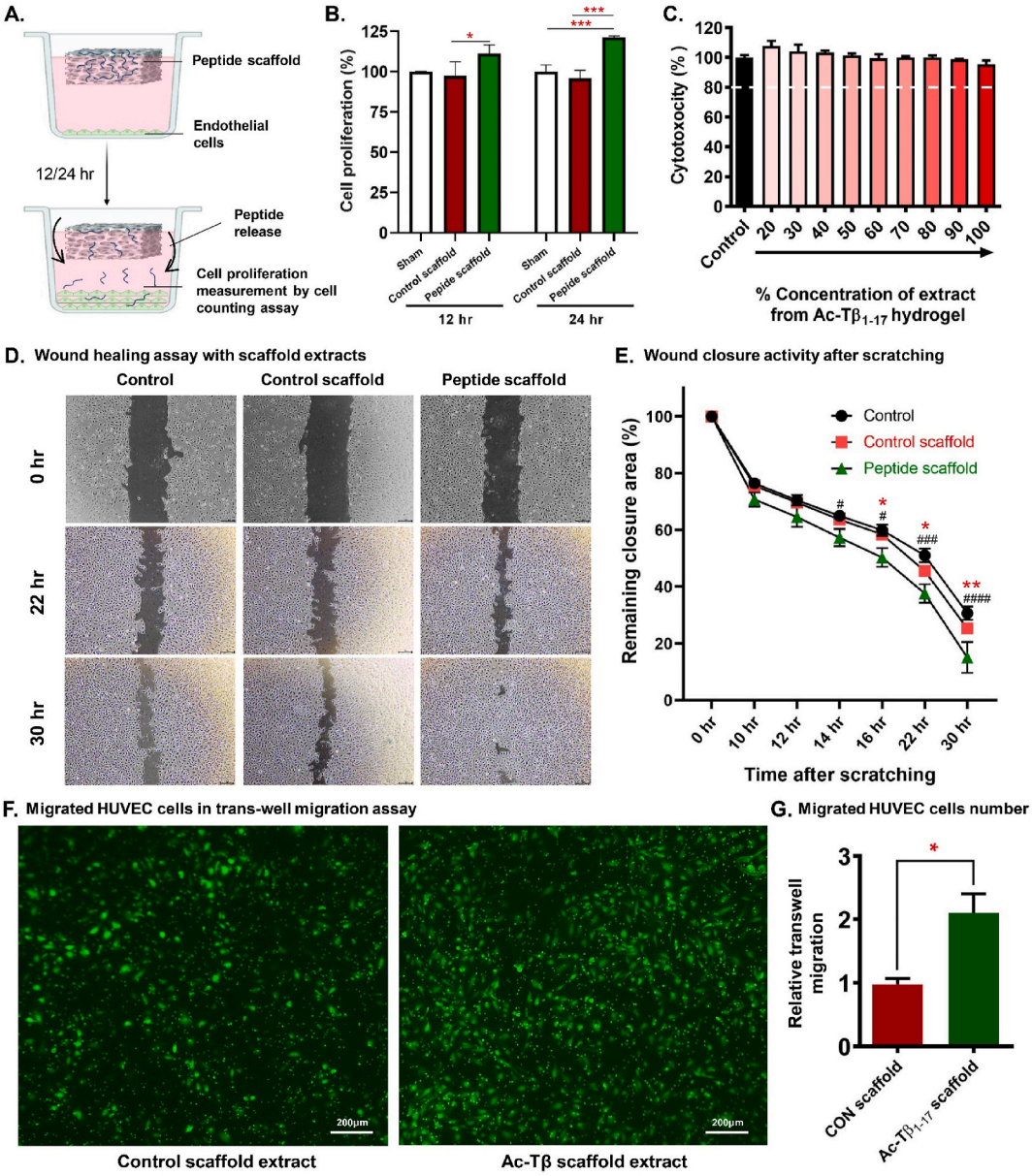


**Fig. 7.** Peptide releasing scheme of Ac-Tβ$_{1-17}$-integrated scaffold (A). Level of cell proliferation after the incubation of human umbilical vein endothelial cells (HUVECs) with control and Ac-Tβ$_{1-17}$ scaffolds floating on the media (B). Cell cytotoxicity is measured using various concentrations of the scaffold extracts collected after 24 h (C). A wound healing assay is performed using regular media (control), 100 % control scaffold extract, and 100 % Ac-Tβ$_{1-17}$ scaffold (D). Wound closure activity is measured by calculating the remaining closure area compared to the individual's 0 h area. A two-way ANOVA was conducted to determine the differences between groups (n = 4) ("#" indicates significance between control and peptide scaffold, and "*" indicates significance between control scaffold and peptide scaffold) (E). Migrated HUVECs in Transwell migration assay are assessed using calcein acetoxymethyl ester (AM) staining and fluorescence microscope (F). The relative number of migrated cells is compared with that of the control scaffold (G). The data are presented as the mean ± SEM, with three samples per group. A p-value is considered statistically significant for all tests (Student's t-test; *p < 0.05, **p < 0.01, ***p < 0.001).

### 3.8. Biocompatibility of peptide scaffold increased proliferation and tube formation of HUVECs

The biocompatibility of the Ac-Tβ$_{1-17}$ peptide scaffold significantly enhanced the proliferation and angiogenic capabilities of HUVECs. To assess these effects, HUVECs were cultured on Ac-Tβ$_{1-17}$ peptide scaffolds (Fig. 8A), and their proliferation was evaluated using a cell counting kit (Fig. 8B). The cultured cells were stained with calcein-AM. The results showed a significant increase in the number of live cells on the scaffold compared to controls without the peptide (Fig. 8C). Fluorescence microscopy visualized increased cell proliferation on the scaffold. Cell numbers were quantified using ImageJ software, showing a significant increase in cell count compared to the control group (Fig. 8D).

Moreover, the angiogenic potential was assessed using a tube formation assay (Fig. 8E). HUVECs cultured on the Ac-Tβ$_{1-17}$ peptide scaffold exhibited enhanced tube formation, indicating increased angiogenic activity (Fig. 8F). Angiogenesis parameters such as tube

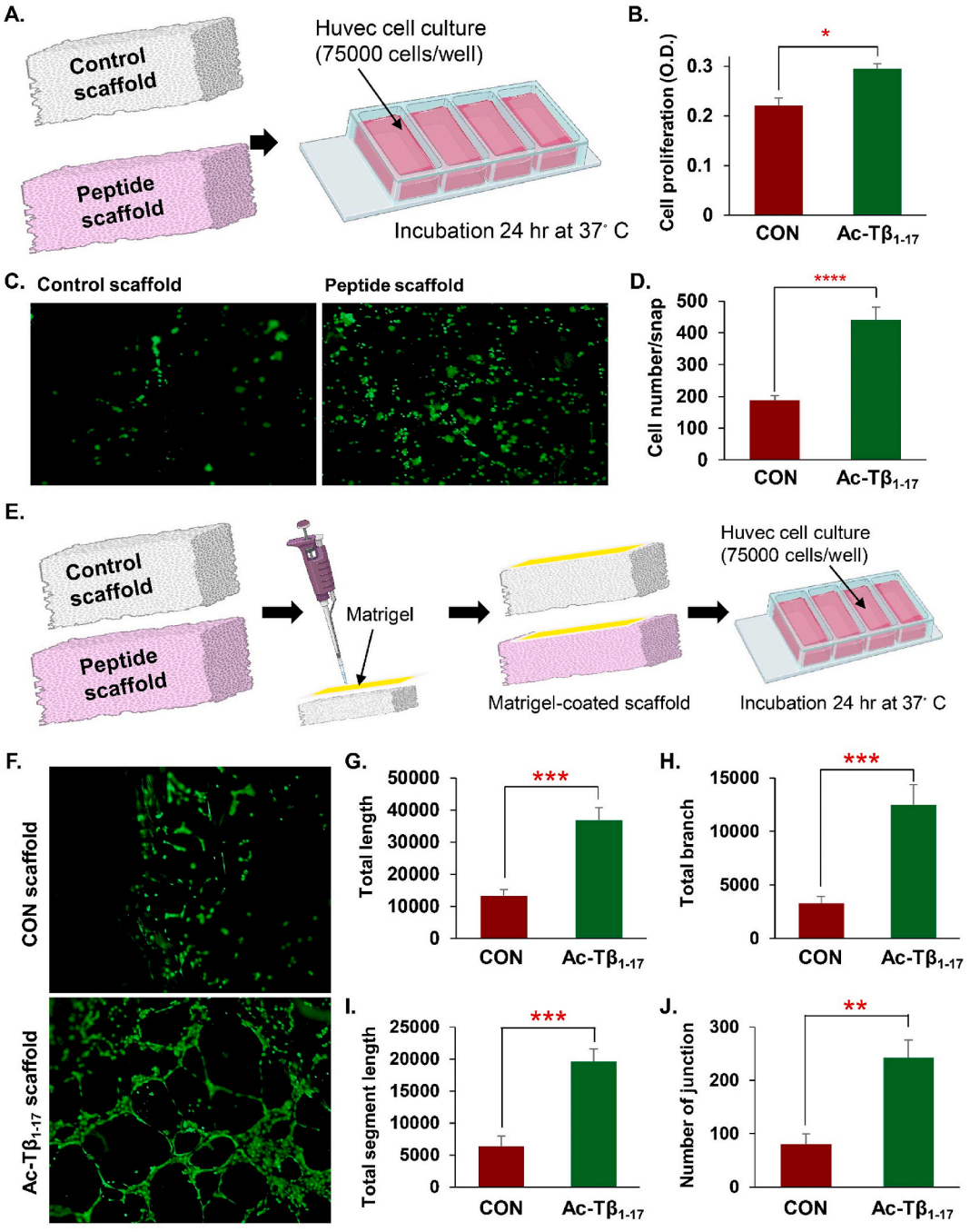


**Fig. 8. Effects of the acetyl-thymosin β4 (1–17) (Ac-Tβ$_{1-17}$) scaffold on cell proliferation and angiogenesis**. Scheme of human umbilical vein endothelial cells (HUVECs) cultured on the scaffold (A). Cell proliferation is measured using calcein acetoxymethyl ester (AM) staining of cells cultured on the scaffold with or without the Ac-Tβ$_{1-17}$ peptide (B). Live cells on the scaffold are imaged using a fluorescence microscope (C). Cell numbers were quantified using ImageJ software (D). Scheme of human umbilical vein endothelial cells (HUVECs) tube formation assay on the scaffold (E). Tube formation is assessed using calcein AM staining of cells cultured on the scaffold with or without the Ac-Tβ$_{1-17}$ peptide (F). The total length, branch, segment length, and number of junctions on the scaffold with or without the Ac-Tβ$_{1-17}$ peptide were analyzed (G–J). The data are presented as the mean ± SEM, with three samples per group. A p-value is considered statistically significant for all tests (Student's t-test; *p < 0.05, **p < 0.01, ***p < 0.001).

length, total branch length, total segment length, and the number of junctions were significantly increased on the peptide scaffold (Fig. 8G–J). Angiogenesis is crucial for wound healing as it facilitates the delivery of oxygen, nutrients, and growth factors through newly formed blood vessels. Additionally, neovascularization supports initial hemostasis and reduces blood loss [57]. The assay results correlated with the proliferation findings, further supporting that the Ac-Tβ$_{1\text{-}17}$ peptide scaffold is a promising biomaterial for enhancing endothelial cell function, which could contribute to improved vascularization in tissue-engineering applications.

### 3.9. Increased production of cell proliferation and angiogenesis-related proteins following Ac-Tβ$_{1\text{-}17}$ treatment in HUVECs

Protein expression in Ac-Tβ$_{1\text{-}17}$-treated HUVECs was assessed by collecting total protein after 24 h of proliferation (with or without the addition of 25 μg/mL Ac-Tβ$_{1\text{-}17}$ peptide) (Fig. 9A). Principal component analysis (PCA) comparing the control and Ac-Tβ$_{1\text{-}17}$-treated groups

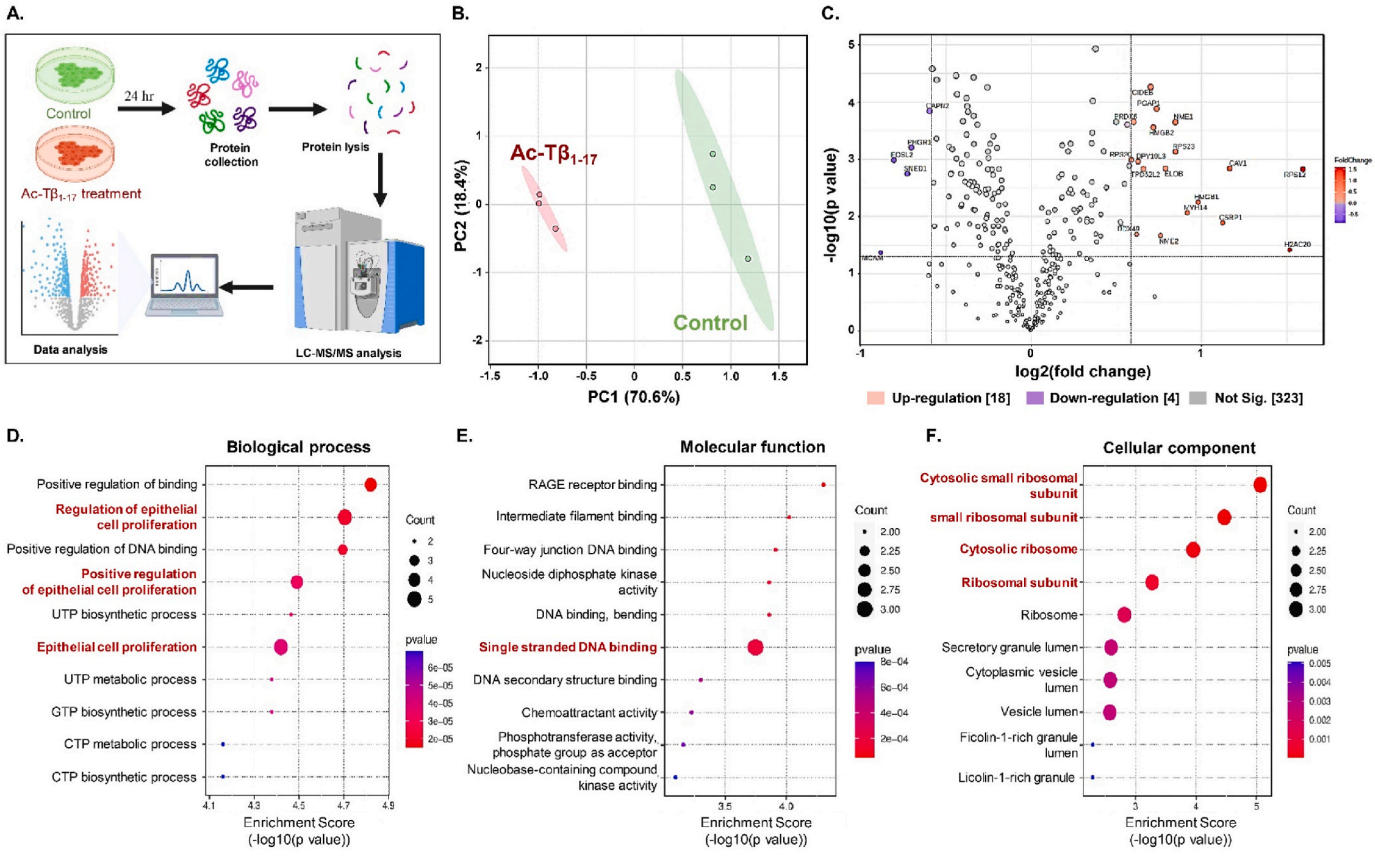


**G. Up-regulated proteins and related pathways**

| Up-regulation | Fold change | p Value | Related pathways |
|---|---|---|---|
| RPS12 | 3 | 0.002 | Cytoplasmic ribosomal proteins (40S) |
| H2AC20 | 2.9 | 0.038 | Novel regulator of proliferation (EGFR pathway) |
| CSRP1 | 2.2 | 0.013 | VEGF-VEGFR pathway |
| CAV1 | 2.2 | 0.001 | VEGF-VEGFR pathway, Evading growth suppressors |
| HMGB1 | 2 | 0.006 | VEGF-VEGFR pathway, Inducing angiogenesis, Evading growth suppressors |
| MYH14 | 1.9 | 0.009 | Cell adhesion Integrin-mediated cell adhesion and migration |
| RPS23 | 1.8 | 0.001 | Initiation of translation, Cytoplasmic ribosomal proteins (40S) |
| NME1 | 1.8 | 0.000 | C-MYC transcriptional activation |
| ELOB | 1.7 | 0.001 | Hypoxic and oxygen homeostasis regulation of HIF-1-alpha |
| NME2 | 1.7 | 0.021 | C-MYC transcriptional activation |
| PGAP1 | 1.7 | 0.000 | Inositol deacylation of GPI-anchored proteins |
| HMGB2 | 1.6 | 0.000 | Evading growth suppressors |
| CIDEB | 1.6 | 0.000 | TGF? signaling pathway |
| TPD52L2 | 1.6 | 0.002 | Regulation of cell population proliferation |
| DPY19L3 | 1.5 | 0.001 | Mediates C-mannosylation of tryptophan residues on target proteins |
| DDX49 | 1.5 | 0.020 | Positive regulation of cell growth |
| PRDX6 | 1.5 | 0.000 | VEGF-VEGFR pathway, Inducing angiogenesis |
| RPS20 | 1.5 | 0.001 | Initiation of translation, Cytoplasmic ribosomal proteins (40S) |

**H. Probable scheme for cell proliferation and angiogenesis**

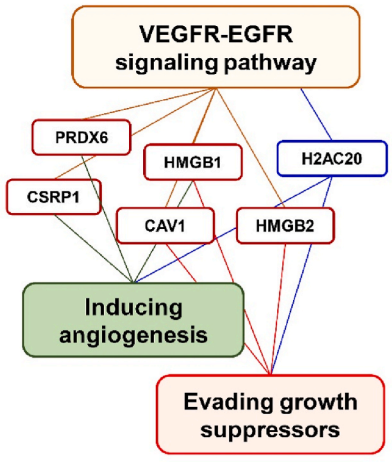


**Fig. 9. Protein expression assessment of acetyl-thymosin β4 (1–17) (Ac-Tβ$_{1\text{-}17}$)-treated human umbilical vein endothelial cells (HUVECs).** Proteomic scheme of Ac-Tβ$_{1\text{-}17}$ peptide-treated HUVECs (A). The principal component analysis (PCA) score plot comparing the control and. Ac-Tβ$_{1\text{-}17}$ treatment groups (B). Volcano plot of upregulated and downregulated protein genes in control vs. Ac-Tβ$_{1\text{-}17}$-treated HUVECs (C). Gene Ontology (GO) enrichment pathway assessment of upregulated proteins identified from Ac-Tβ$_{1\text{-}17}$ treatment (D–F). List of pregulated proteins and their associated proteins in control vs. Ac-Tβ$_{1\text{-}17}$-treated HUVECs (G). Scheme of upregulated proteins associated with angiogenesis (H).

revealed a distinct separation between the two groups based on protein expression (Fig. 9B). Protein screening was conducted based on the criteria of a p-value <0.05- and 1.5-fold change, resulting in a volcano plot (Fig. 9C). This analysis identified 18 significantly upregulated and four downregulated proteins in the Ac-T$\beta_{1\text{-}17}$-treated group compared to those in the control group. GO enrichment pathway analysis of upregulated proteins revealed significant increases in biological processes, such as the regulation of epithelial cell proliferation and positive regulation of epithelial cell proliferation following Ac-T$\beta_{1\text{-}17}$ treatment (Fig. 9D). The upregulated proteins were associated with molecular functions, such as single-stranded DNA binding and cellular components.

After Ac-T$\beta_{1\text{-}17}$ peptide treatment, analysis of the upregulated proteins through gene cards and GO enrichment pathways revealed a 3-fold increase in cytoplasmic ribosomal proteins (40s), similar to the small ribosomal subunit involved in cell proliferation and angiogenesis (Fig. 9E & F). After Ac-T$\beta_{1\text{-}17}$ peptide treatment, researchers observed a 2.9-fold increase in H2AC20 protein (Fig. 9G). Previously, researchers have observed that H2AC20 ubiquitination is regulated by the epidermal growth factor receptor (EGFR) pathway [58]. Based on this evidence, Ac-T$\beta_{1\text{-}17}$ peptide treatment likely activated the EGFR pathway and simultaneously increased H2AC20 protein levels in the HUVECs. Additionally, the EGFR pathway is closely associated with the vascular endothelial growth factor receptor (VEGFR) pathway and can affect vice-versa through crosstalk [59]. In this study, proteins closely associated with the VEGF-VEGFR pathway, such as cysteine and glycine-rich protein 1 (CSRP1), peroxiredoxin 6 (PRDX6), high mobility group box 1 protein (HMGB1), and caveolin-1 (CAV1), were upregulated after Ac-T$\beta_{1\text{-}17}$ peptide treatment (Fig. 9G & H). CSRP1, PRDX6, and HMGB1 were associated with the induction of cell angiogenesis. Additionally, proteins (HMGB1, HMGB2 [60], and CAV1) involved in evading growth suppression were upregulated.

The findings from this study offer intriguing insights into the biological effect of Ac-T$\beta_{1\text{-}17}$ peptide on endothelial cell behavior, specifically highlighting its role in enhancing cell proliferation and angiogenesis. The significant upregulation of proteins associated with the EGFR-VEGFR pathway, such as H2AC20, CSRP1 [61], PRDX6, HMGB1, and CAV1 [62], highlights the potential of Ac-T$\beta_{1\text{-}17}$ as a regulator of angiogenic processes. This pathway is crucial for vascular development and repair [63], indicating that Ac-T$\beta_{1\text{-}17}$ may offer promising therapeutic benefits for enhancing angiogenesis, such as wound healing and cardiovascular diseases. The potential of Ac-T$\beta_{1\text{-}17}$ in regenerative medicine and tissue engineering indicates promising future treatments.

### 3.10. Increased expression of cell growth, proliferation, and migration genes following Ac-T$\beta_{1\text{-}17}$ treatment in HUVECs

Gene expression analysis revealed the potential of the Ac-T$\beta_{1\text{-}17}$ peptide to effectively regulate various pathways. The expression of cell proliferation-associated genes, such as protein kinase B (Akt), extracellular signal-regulated kinase (ERK)1/2, mitogen-activated protein kinase (MEK), and phosphoinositide 3-kinase (PI3K), were significantly increased following Ac-T$\beta_{1\text{-}17}$ peptide treatment (25 μg/mL) for 24 h compared to the control groups (Fig. 10A–D). The treatment of Ac-T$\beta_{1\text{-}17}$ peptide also increased B-cell lymphoma 2 (Bcl-2) gene expression (Fig. 10E). Additionally, Bcl-2-associated X protein (BAX) expression was reduced compared to the control group, but not significantly (Fig. 10F). Interestingly, BAX/Bcl-2 ratio was significantly down regulated (Fig. 10G), indicating a shift towards apoptotic regulation, favoring cell survival under stress conditions.

This analysis demonstrated that significant signaling pathways, including PI3K-AKT and MEK-ERK1/2, were upregulated through Ac-T$\beta_{1\text{-}17}$ treatment. PI3K-AKT and MEK-ERK1/2 are significantly associated with EGFR-VEGFR pathways [64,65]. Similar patterns of gene expression were observed when the mRNA from HUVECs treated with the control and Ac-T$\beta_{1\text{-}17}$ scaffold extracts were assessed (Fig. 10H–N). Gene expression analysis showed that Ac-T$\beta_{1\text{-}17}$ peptide upregulated crucial pathways, including Bax and Bcl-2, resulting in a significant decrease in the BAX/Bcl-2 expression ratio (Fig. 10I), highlighting a nuanced mechanism of action. This ratio, indicating enhanced anti-apoptotic signaling (Fig. 10O) [66], is paradoxically linked to increased cell proliferation and angiogenesis through increase of Akt, ERK1/2, MEK, and PI3K gene expression. This suggests that Ac-T$\beta_{1\text{-}17}$ balances the cell survival and death pathways to facilitate tissue regeneration. This balance highlights the potential of Ac-T$\beta_{1\text{-}17}$ as a therapeutic agent for regenerative medicine and tissue engineering.

### 3.11. Ex vivo effects of Ac-T$\beta_{1\text{-}17}$ peptide in increased vascularization of fetus metatarsal bone

The fetal mouse metatarsal bone explant is a well-known angiogenesis model [67] (Fig. 11A), which is used exclusively to determine the angiogenic effects of biomaterials and molecules [68]. In this study, the ex vivo application of Ac-T$\beta_{1\text{-}17}$ peptide (25 μg/mL) for 5 days demonstrated significant efficacy in facilitating vascularization, as evidenced by the increased size and enhanced vascular outgrowth in fetal mouse metatarsals (Fig. 11B–C). The significant increase in metatarsal size following Ac-T$\beta_{1\text{-}17}$ peptide treatment highlights the potential of the peptide to stimulate growth. This indicated that Ac-T$\beta_{1\text{-}17}$ can effectively enhance cellular proliferation and tissue expansion, which are crucial for regenerative processes. The significant enhancement in vessel outgrowth supports the proangiogenic properties of Ac-T$\beta_{1\text{-}17}$ peptide (Fig. 11D). The fluorescent images demonstrated extensive vessel networks in the treated samples compared to the controls, highlighting the role of peptides in facilitating endothelial cell proliferation and migration. This aligns with previous studies demonstrating the angiogenic effects of Ac-T$\beta_{1\text{-}17}$ in vitro. Quantitative analysis demonstrated significant increases in vessel-covered area and density following Ac-T$\beta_{1\text{-}17}$ treatment (Fig. 11E–F). Additionally, the number of junctions, total branching length, and total branch length increased compared to those in the control group, offering further insights into the structural enhancements of the vascular networks (Fig. 11G–I). An increase in the number of junctions indicates enhanced vascular network connectivity, which is crucial for efficient blood flow and nutrient distribution. The extended branching length and total branch length observed in the treated groups reflect the potential of the peptide to facilitate extensive angiogenesis, further confirming its therapeutic potential.

Our results demonstrate that increased expression of proteins and genes involved in inducing angiogenesis and evading growth suppression indicates the potential of the peptide to support sustained cellular proliferation, a necessary component of effective tissue regeneration. The ex vivo studies offer compelling evidence of the potential of the Ac-T$\beta_{1\text{-}17}$ peptide to enhance vascularization. These findings indicated that Ac-T$\beta_{1\text{-}17}$ could significantly contribute to therapeutic angiogenesis and tissue engineering applications, offering a promising strategy for enhancing vascularization in regenerative medicine. Our group is currently conducting future studies to explore the underlying mechanisms of action and assess the efficacy of the peptide in in vivo models to further establish its clinical applicability.

However, these molecular insights enhance our understanding of the broader potential of peptide-based therapies [25] and spark interest in exploring protein metabolism to gain a deeper understanding of protein function. In our previous research, we discovered that exposing HUVECs to the original compound resulted in the abundant formation of a specific metabolite within 24 h [29]. This indicates that the inherent activity of the parent peptide can contribute to the observed effects of its metabolite, revealing a previously unrecognized aspect of small peptide functionality [30]. Our study indicates that small peptides and their derivatives may synergistically perform their known biological roles. Although this interplay was not the primary focus of this study, combining our previous findings with our recent results strongly

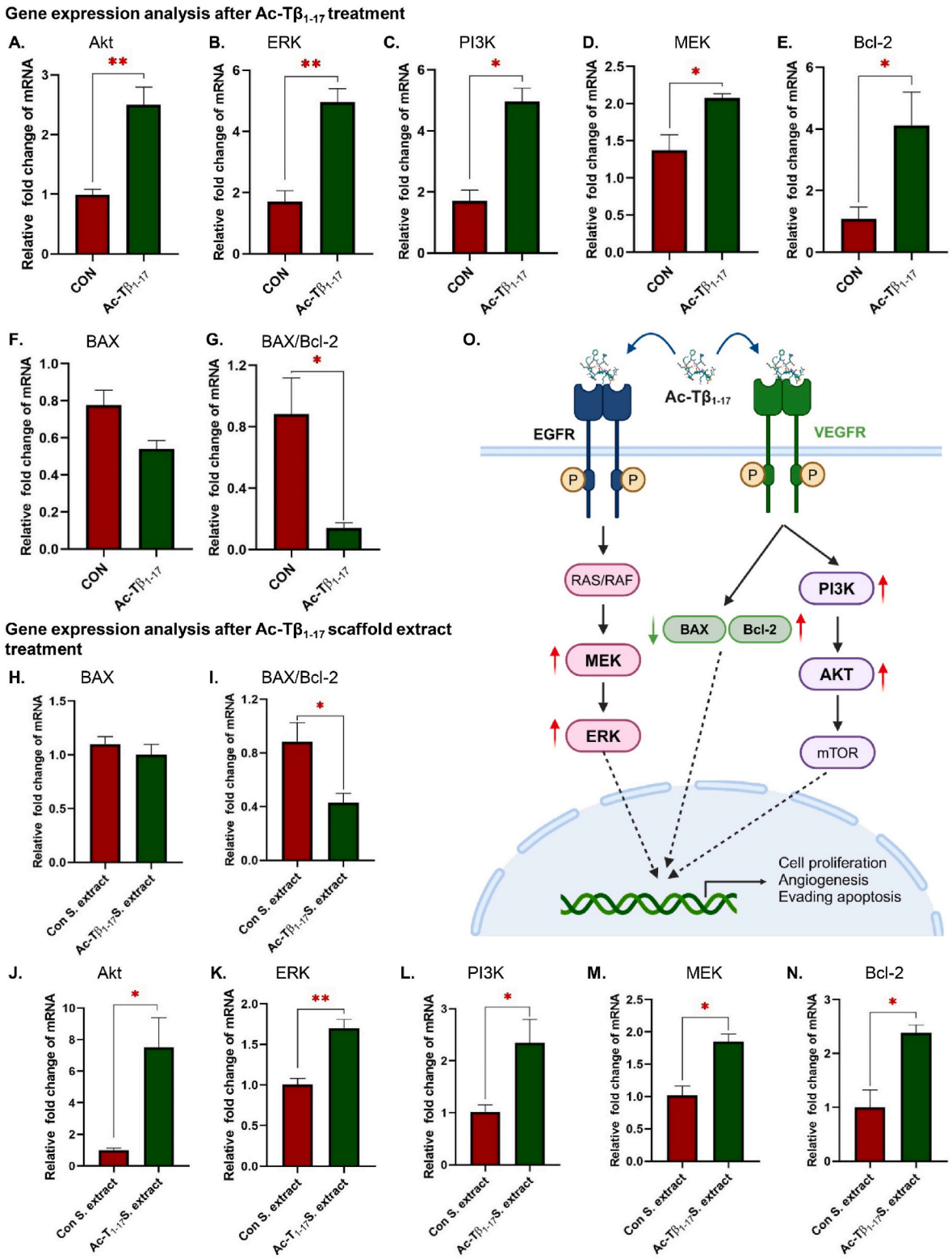


**Fig. 10. Ability of Ac-Tβ$_{1-17}$ peptide to regulate various gene expressions.** Treatment with 25 μg/mL Ac-Tβ$_{1-17}$ peptide for 24 h upregulates protein kinase B (Akt), extracellular signal-regulated kinase (ERK), phosphoinositide 3-kinase (PI3K), MEK and B-cell lymphoma 2 (Bcl-2) gene expression (A–E). Bcl-2-associated X protein (BAX) expression is reduced after Ac-Tβ$_{1-17}$ peptide treatment but is insignificant (F). BAX/Bcl-2 ratio was significantly down regulated (G). Human umbilical vein endothelial cells (HUVECs) are also cultured with 100 % extract from the control scaffold and Ac-Tβ$_{1-17}$ peptide scaffold. Akt, ERK, PI3K, MEK and Bcl-2 gene expression increased significantly (J–N), whereas BAX expression is unaffected (H). But BAX/Bcl-2 ratio was significantly down regulated (I). The molecular mechanism assessed from the study was illustrated in Fig. 10 (O). The data are presented as the mean ± SEM, with three samples per group. A p-value is considered statistically significant for all tests (Student's t-test; *$p < 0.05$, **$p < 0.01$).

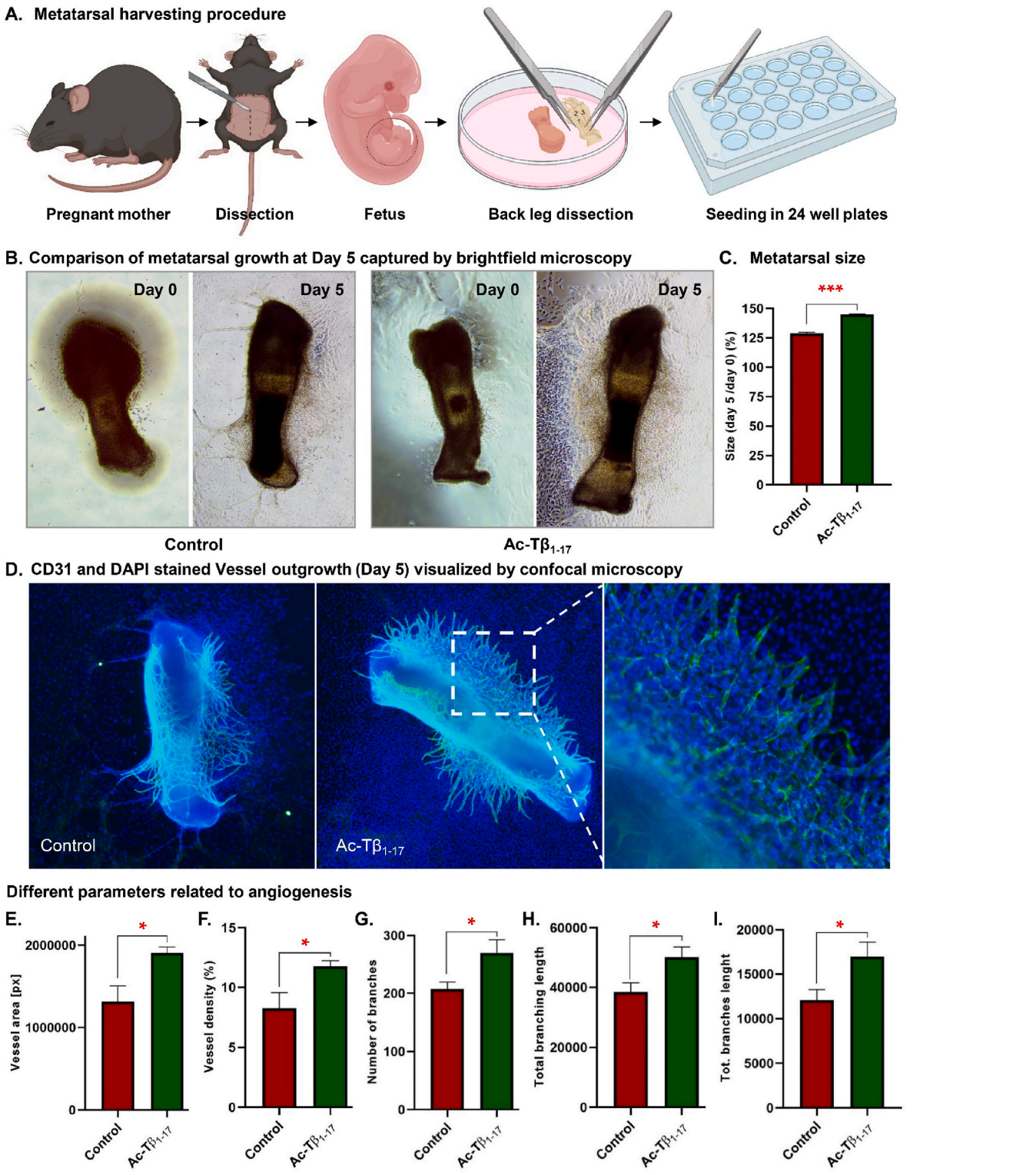


**Fig. 11. Effects of Ac-T$\beta_{1\text{-}17}$ peptide in ex vivo vascularization of fetus metatarsal**. Schematic illustration of fetal mouse metatarsal harvesting procedure (A). Treatment with 25 μg/mL Ac-T$\beta_{1\text{-}17}$ peptide for 5 days significantly increased the metatarsal size (B–C). Representative fluorescent images of CD31 positive vessel outgrowth from metatarsal growth under control and 25 μg/mL Ac-T$\beta_{1\text{-}17}$ peptide treatment conditions (D). Vessel-covered area (%) and vessel density (%) are measured using WimScatch (web-based software from Wimasis) (E–F). ImageJ software measured the number of junctions, total branching length, and total branch length (G–I). The data are presented as the mean ± SEM, with four samples per group. A p-value is considered statistically significant for all tests (Student's t-test; *p < 0.05, **p < 0.01, ***p < 0.001).

indicated that these interactions are feasible within biological systems.

## 4. Conclusions

In conclusion, our study offers compelling evidence for the potential of peptide metabolites, specifically those derived from Tβ4, such as Ac-$T\beta_{1\text{-}17}$, in biomedical applications and biomaterial development. The significant inhibitory activity of Ac-$T\beta_{1\text{-}17}$ against SARS-CoV-2 compared to its parent and its ability to facilitate cell proliferation, wound healing, ROS scavenging, and angiogenesis of HUVECs and fetal mouse metatarsal highlight its therapeutic potential. The integration of Ac-$T\beta_{1\text{-}17}$ into peptide-based scaffolds facilitates their release into the medium and increases cell growth, further highlighting the innovative possibilities in biomaterials science. The Ac-$T\beta_{1\text{-}17}$ treatment induced a broader biochemical response, significantly affecting gene and protein expression in HUVECs, highlighting the intricate interplay between peptide metabolites and cellular mechanisms. Our findings advance the understanding of the role of peptide metabolites in biological systems and offer novel approach for designing and developing more compatible and therapeutic biomaterials. Using the biological activities of peptide metabolites, we can envision a future in which biomaterials enhance healing, facilitate tissue regeneration, and combat pathogens effectively. This study opens avenues for exploring peptide metabolites in biomaterials that offer enhanced compatibility and therapeutic efficacy across medical applications.

## CRediT authorship contribution statement

**Khandoker Asiqur Rahaman:** Writing – original draft, Investigation, Formal analysis, Data curation, Conceptualization. **Md Sofequl Islam Mukim:** Writing – original draft, Investigation, Data curation. **Md Lemon Hasan:** Writing – original draft, Investigation. **Hyeok Kim:** Writing – original draft, Methodology, Investigation. **Cheol-Ho Pan:** Validation, Supervision, Conceptualization. **Oh-Seung Kwon:** Resources, Formal analysis, Data curation. **Dae-Geun Song:** Writing – original draft, Validation, Project administration. **Hyung-Seop Han:** Writing – original draft, Validation, Supervision, Project administration, Funding acquisition, Conceptualization.

## Ethics approval and consent to participate

No human subjects and clinical samples were involved in the reported work. The use and care of experimental animals were approved by the institutional animal ethics committee of the Korea Institute of Science and Technology (KIST-IACUC-2025-001).

## Declarations of competing interest

Hyung-Seop Han is an editorial board member for Bioactive Materials and was not involved in the editorial review or the decision to publish this article. The authors declare the following personal relationships which may be considered as potential competing interests: Hyung-Seop Han is currently employed by Elecell Corporation.

## Acknowledgments

This work was supported by the National Research Foundation (NRF) grant funded by the Korean government (NRF-2021K1A3A1A74095929, NRF-2021R1A2C2092375), a Korea Research Council (NRF-2022M3H4A1A0407327112), the intramural grant from the Korea Institute of Science and Technology (Grand Challenge, 2Z07012 and Open Research Program, 2E33311), and Korea National University of Science and Technology grant 2021YS16. The figures were created using BioRender.com.

## Appendix A. Supplementary data

Supplementary data to this article can be found online at https://doi.org/10.1016/j.bioactmat.2025.02.008.

## References

[1] M. Su, Y. Ling, J. Yu, J. Wu, J. Xiao, Small proteins: untapped area of potential biological importance, Front. Genet. 4 (2013) 286.
[2] I.W. Hamley, Small bioactive peptides for biomaterials Design and therapeutics, Chem Rev 117 (24) (2017) 14015–14041.
[3] J.I. Lachowicz, G. Pichiri, M. Piludu, S. Fais, G. Orru, T. Congiu, M. Piras, G. Faa, D. Fanni, G. Dalla Torre, X. Lopez, K. Chandra, K. Szczepski, L. Jaremko, M. Ghosh, A.H. Emwas, M. Castagnola, M. Jaremko, E. Hannappel, P. Coni, Thymosin beta4 is an endogenous Iron Chelator and molecular Switcher of Ferroptosis, Int. J. Mol. Sci. 23 (1) (2022).
[4] G. Sosne, P. Qiu, A.L. Goldstein, M. Wheater, Biological activities of thymosin beta4 defined by active sites in short peptide sequences, FASEB J. 24 (7) (2010) 2144–2151.
[5] Y. Xing, Y. Ye, H. Zuo, Y. Li, Progress on the function and application of thymosin beta4, Front. Endocrinol. 12 (2021) 767785.
[6] I. Bock-Marquette, K. Maar, S. Maar, B. Lippai, G. Faskerti, F. Gallyas Jr., E. N. Olson, D. Srivastava, Thymosin beta-4 denotes new directions towards developing prosperous anti-aging regenerative therapies, Int. Immunopharmacol. 116 (2023) 109741.
[7] M.R. Garvin, C. Alvarez, J.I. Miller, E.T. Prates, A.M. Walker, B.K. Amos, A.E. Mast, A. Justice, B. Aronow, D. Jacobson, A mechanistic model and therapeutic interventions for COVID-19 involving a RAS-mediated bradykinin storm, Elife 9 (2020).
[8] R.G.H. Lindeboom, K.B. Worlock, L.M. Dratva, M. Yoshida, D. Scobie, H. R. Wagstaffe, L. Richardson, A. Wilbrey-Clark, J.L. Barnes, L. Kretschmer, K. Polanski, J. Allen-Hyttinen, P. Mehta, D. Sumanaweera, J.M. Boccacino, W. Sungnak, R. Elmentaite, N. Huang, L. Mamanova, R. Kapuge, L. Bolt, E. Prigmore, B. Killingley, M. Kalinova, M. Mayer, A. Boyers, A. Mann, L. Swadling, M.N.J. Woodall, S. Ellis, C.M. Smith, V.H. Teixeira, S.M. Janes, R.C. Chambers, M. Haniffa, A. Catchpole, R. Heyderman, M. Noursadeghi, B. Chain, A. Mayer, K. B. Meyer, C. Chiu, M.Z. Nikolić, S.A. Teichmann, Human SARS-CoV-2 challenge uncovers local and systemic response dynamics, Nature 631 (8019) (2024) 189–198.
[9] Z. Jin, X. Du, Y. Xu, Y. Deng, M. Liu, Y. Zhao, B. Zhang, X. Li, L. Zhang, C. Peng, Y. Duan, J. Yu, L. Wang, K. Yang, F. Liu, R. Jiang, X. Yang, T. You, X. Liu, X. Yang, F. Bai, H. Liu, X. Liu, L.W. Guddat, W. Xu, G. Xiao, C. Qin, Z. Shi, H. Jiang, Z. Rao, H. Yang, Structure of M(pro) from SARS-CoV-2 and discovery of its inhibitors, Nature 582 (7811) (2020) 289–293.
[10] A.M. Shaqra, S.N. Zvornicanin, Q.Y.J. Huang, G.J. Lockbaum, M. Knapp, L. Tandeske, D.T. Bakan, J. Flynn, D.N.A. Bolon, S. Moquin, D. Dovala, N. Kurt Yilmaz, C.A. Schiffer, Defining the substrate envelope of SARS-CoV-2 main protease to predict and avoid drug resistance, Nat. Commun. 13 (1) (2022) 3556.
[11] T. Xu, J. Wang, S. Zhao, D. Chen, H. Zhang, Y. Fang, N. Kong, Z. Zhou, W. Li, H. Wang, Accelerating the prediction and discovery of peptide hydrogels with human-in-the-loop, Nat. Commun. 14 (1) (2023) 3880.
[12] R.J. Malonis, J.R. Lai, O. Vergnolle, Peptide-based vaccines: current progress and future challenges, Chem Rev 120 (6) (2020) 3210–3229.
[13] M. Pavlicevic, N. Marmiroli, E. Maestri, Immunomodulatory peptides-A promising source for novel functional food production and drug discovery, Peptides 148 (2022) 170696.
[14] M. Dadar, Y. Shahali, S. Chakraborty, M. Prasad, F. Tahoori, R. Tiwari, K. Dhama, Antiinflammatory peptides: current knowledge and promising prospects, Inflamm. Res. 68 (2) (2019) 125–145.
[15] S.M. Chowdhury, S.A. Talukder, A.M. Khan, N. Afrin, M.A. Ali, R. Islam, R. Parves, A. Al Mamun, M.A. Sufian, M.N. Hossain, M.A. Hossain, M.A. Halim, Antiviral peptides as promising therapeutics against SARS-CoV-2, J. Phys. Chem. B 124 (44) (2020) 9785–9792.
[16] P.V. Bagwe, P.V. Bagwe, S.S. Ponugoti, S.V. Joshi, Peptide-based vaccines and therapeutics for COVID-19, Int J Pept Res Ther 28 (3) (2022) 94.
[17] B.C. Goncalves, M.G. Lopes Barbosa, A.P. Silva Olak, N. Belebecha Terezo, L. Nishi, M.A. Watanabe, P. Marinello, D. Zendrini Rechenchoski, S.P. Dejato Rocha, L. C. Faccin-Galhardi, Antiviral therapies: advances and perspectives, Fundam. Clin. Pharmacol. 35 (2) (2021) 305–320.
[18] C.A.G. Amelia, J.C. Helen, H. Rose, N. Linda, M. Viyaasan, M.S. Rebecca, M. Amir, I. Peter, D. Henry, J.D. Nicholas, C. Richard, T.R. Christopher, B. Krishnan, T. John, Z. Bang, D.A. Colm, C.J.B. Sebastian, D. Simon, D. Iain, E. David, F. Louis, H. George, E.M.H. Lisa, J.H. William, M. Jon, M. Orla, M. Jessica, E.M. Caroline, Y. P. Robin, J.W. Alex, W. Tom, W. Milan, B. Christopher, C. Jonathan, P. John, H. Frank, H. Sam, J.D. Ian, J.W.E. Stephen, G. Ben, A.T. Laurie, M. Brian, Trends, variation, and clinical characteristics of recipients of antiviral drugs and neutralising monoclonal antibodies for covid-19 in community settings: retrospective, descriptive cohort study of 23.4 million people in OpenSAFELY, BMJ Medicine 2 (1) (2023) e000276.
[19] S. Jiang, Editorial: peptide-based immunotherapy against emerging viral infections, Front. Immunol. 14 (2023).
[20] S. Park, K.A. Rahaman, Y.C. Kim, H. Jeon, H.S. Han, Fostering tissue engineering and regenerative medicine to treat musculoskeletal disorders in bone and muscle, Bioact. Mater. 40 (2024) 345–365.

[21] M.L. Hasan, J.R. Lee, K.A. Rahaman, D.H. Yang, Y.K. Joung, Versatile effects of galectin-1 protein-containing lipid bilayer coating for cardiovascular applications, Bioact. Mater. 42 (2024) 207–225.
[22] Z. Lotfollahi, J. Dawson, R. Fitridge, C. Bursill, The anti-inflammatory and proangiogenic properties of high-density Lipoproteins: an emerging role in diabetic wound healing, Adv. Wound Care 10 (7) (2021) 370–380.
[23] T. Liang, J. Liu, F. Liu, X. Su, X. Li, J. Zeng, F. Chen, H. Wen, Y. Chen, J. Tao, Q. Lei, G. Li, P. Cheng, Application of pro-angiogenic biomaterials in Myocardial Infarction, ACS Omega 9 (36) (2024) 37505–37529.
[24] A.H. Van Hove, K. Burke, E. Antonienko, E. Brown, D.S.W. Benoit, Enzymatically-responsive pro-angiogenic peptide-releasing poly(ethylene glycol) hydrogels promote vascularization in vivo, J. Contr. Release 217 (2015) 191–201.
[25] L. Wang, N. Wang, W. Zhang, X. Cheng, Z. Yan, G. Shao, X. Wang, R. Wang, C. Fu, Therapeutic peptides: current applications and future directions, Signal Transduct. Targeted Ther. 7 (1) (2022) 48.
[26] L. De Rosa, R. Di Stasi, L.D. D'Andrea, Pro-angiogenic peptides in biomedicine, Arch. Biochem. Biophys. 660 (2018) 72–86.
[27] M.T. Ngo, B.A.C. Harley, Angiogenic biomaterials to promote therapeutic regeneration and investigate disease progression, Biomaterials 255 (2020) 120207.
[28] K.A. Rahaman, A.R. Muresan, H. Min, J. Son, M.-J. Kang, O.-S. Kwon, An approach for identifying in silico peptides against authentic metabolites: in vitro characterization of thymosin β4 metabolites, Journal of Pharmaceutical Investigation 52 (5) (2022) 611–621.
[29] K.A. Rahaman, A.R. Muresan, M.L. Hasan, Y.K. Joung, H. Min, J. Son, M.J. Kang, O.S. Kwon, Detection and quantification of the metabolite Ac-Tbeta(1-14) in in vitro experiments and urine of rats treated with Ac-Tbeta4: a potential biomarker of Ac-Tbeta4 for doping tests, Drug Test. Anal. (2023).
[30] K.A. Rahaman, A.R. Muresan, H. Min, J. Son, H.-S. Han, M.-J. Kang, O.-S. Kwon, Simultaneous quantification of TB-500 and its metabolites in in-vitro experiments and rats by UHPLC-Q-Exactive orbitrap MS/MS and their screening by wound healing activities in-vitro, J. Chromatogr. B 1235 (2024) 124033.
[31] J. Ke, J. Zhang, J. Li, J. Liu, S. Guan, Design of Cyclic peptide-based Nanospheres and the delivery of siRNA, Int. J. Mol. Sci. (2022).
[32] I.P. Sæbø, M. Bjørås, H. Franzyk, E. Helgesen, J.A. Booth, Optimization of the hemolysis assay for the assessment of cytotoxicity, Int. J. Mol. Sci. (2023).
[33] M. Morais, P. Tian, R. O'Cualain, C. Lawless, R. Lennon, Protocol to characterize basement membranes during kidney development using mass spectrometry-based label-free quantitative proteomics, STAR Protoc 4 (4) (2023) 102741.
[34] Z. Pang, G. Zhou, J. Ewald, L. Chang, O. Hacariz, N. Basu, J. Xia, Using MetaboAnalyst 5.0 for LC–HRMS spectra processing, multi-omics integration and covariate adjustment of global metabolomics data, Nat. Protoc. 17 (8) (2022) 1735–1761.
[35] D. Tang, M. Chen, X. Huang, G. Zhang, L. Zeng, G. Zhang, S. Wu, Y. Wang, SRplot: a free online platform for data visualization and graphing, PLoS One 18 (11) (2023) e0294236.
[36] A.M. Khan, W. Atia Tul, S. Farooq, A. Ullah, M.I. Choudhary, Repurposing of US-FDA approved drugs against SARS-CoV-2 main protease (M(pro)) by using STD-NMR spectroscopy, in silico studies and antiviral assays, Int. J. Biol. Macromol. 234 (2023) 123540.
[37] J. Eberhardt, D. Santos-Martins, A.F. Tillack, S. Forli, AutoDock Vina 1.2.0: new docking methods, Expanded Force field, and Python bindings, J. Chem. Inf. Model. 61 (8) (2021) 3891–3898.
[38] S. Guo, S. Qiu, Y. Cai, Z. Wang, Q. Yang, S. Tang, Y. Xie, A. Zhang, Mass spectrometry-based metabolomics for discovering active ingredients and exploring action mechanism of herbal medicine, Front. Chem. 11 (2023).
[39] M. Thevis, T. Kuuranne, H. Geyer, Annual banned-substance review 16(th) edition-Analytical approaches in human sports drug testing 2022/2023, Drug Test. Anal. 16 (1) (2024) 5–29.
[40] B.J. Bruno, G.D. Miller, C.S. Lim, Basics and recent advances in peptide and protein drug delivery, Ther. Deliv. 4 (11) (2013) 1443–1467.
[41] F. Sheehan, D. Sementa, A. Jain, M. Kumar, M. Tayarani-Najjaran, D. Kroiss, R. V. Ulijn, Peptide-based Supramolecular systems Chemistry, Chem. Rev. 121 (22) (2021) 13869–13914.
[42] L. Wang, N. Wang, W. Zhang, X. Cheng, Z. Yan, G. Shao, X. Wang, R. Wang, C. Fu, Therapeutic peptides: current applications and future directions, Signal Transduct Target Ther 7 (1) (2022) 48.
[43] X. Wang, L. Liu, L. Qi, C. Lei, P. Li, Y. Wang, C. Liu, H. Bai, C. Han, Y. Sun, J. Liu, A first-in-human, randomized, double-blind, single- and multiple-dose, phase I study of recombinant human thymosin beta4 in healthy Chinese volunteers, J. Cell Mol. Med. 25 (17) (2021) 8222–8228.
[44] I. Antonopoulou, E. Sapountzaki, U. Rova, P. Christakopoulos, Inhibition of the main protease of SARS-CoV-2 (M(pro)) by repurposing/designing drug-like substances and utilizing nature's toolbox of bioactive compounds, Comput. Struct. Biotechnol. J. 20 (2022) 1306–1344.
[45] P.T. Djouonzo, M.S.I. Mukim, P.N. Kemda, T.K. Kowa, A.T. Tchinda, G. Agbor Agbor, C.-H. Pan, D.-G. Song, SARS-CoV-2 main protease inhibitors from the stem barks of Discoglypremna caloneura (Pax) Prain (Euphorbiaceae) and Pterocarpus erinaceus Poir (Fabaceae) and their molecular docking investigation, Applied Biological Chemistry 66 (1) (2023) 76.
[46] H. Su, Y. Xu, Application of ITC-based characterization of thermodynamic and kinetic association of ligands with proteins in drug Design, Front. Pharmacol. 9 (2018) 1133.
[47] J.A. Motyan, M. Mahdi, G. Hoffka, J. Tozser, Potential resistance of SARS-CoV-2 main protease (Mpro) against protease inhibitors: Lessons Learned from HIV-1 protease, Int. J. Mol. Sci. 23 (7) (2022).
[48] Y. Xiong, Y. Zhang, A. Mahmood, Y. Meng, Z.G. Zhang, D.C. Morris, M. Chopp, Neuroprotective and neurorestorative effects of thymosin beta4 treatment initiated 6 hours after traumatic brain injury in rats, J. Neurosurg. 116 (5) (2012) 1081–1092.
[49] D. Philp, T. Huff, Y.S. Gho, E. Hannappel, H.K. Kleinman, The actin binding site on thymosin beta4 promotes angiogenesis, FASEB J. 17 (14) (2003) 2103–2105.
[50] P. Chaudhary, P. Janmeda, A.O. Docea, B. Yeskaliyeva, A.F. Abdull Razis, B. Modu, D. Calina, J. Sharifi-Rad, Oxidative stress, free radicals and antioxidants: potential crosstalk in the pathophysiology of human diseases, Front. Chem. 11 (2023).
[51] A. Guru, C. Lite, A.J. Freddy, P.K. Issac, M. Pasupuleti, N.T. Saraswathi, M. V. Arasu, N.A. Al-Dhabi, A. Arshad, J. Arockiaraj, Intracellular ROS scavenging and antioxidant regulation of WL15 from cysteine and glycine-rich protein 2 demonstrated in zebrafish in vivo model, Dev. Comp. Immunol. 114 (2021) 103863.
[52] J.H. Collier, T. Segura, Evolving the use of peptides as components of biomaterials, Biomaterials 32 (18) (2011) 4198–4204.
[53] A. Aravamudhan, M.R. Daisy, J. Nip, A. Subramanian, R. James, D.H. Matthew, X. Yu, G.K. Sangamesh, Osteoinductive small molecules: growth factor alternatives for bone tissue engineering, Curr. Pharm. Des. 19 (19) (2013) 3420–3428.
[54] N. Guan, Z. Liu, Y. Zhao, Q. Li, Y. Wang, Engineered biomaterial strategies for controlling growth factors in tissue engineering, Drug Deliv. 27 (1) (2020) 1438–1451.
[55] C.J.C. Edwards-Gayle, J.K. Wychowaniec, Characterization of peptide-based nanomaterials, in: M.A. Elsawy (Ed.), Peptide Bionanomaterials: from Design to Application, Springer International Publishing, Cham, 2023, pp. 255–308.
[56] M. Koerselman, L.C.M. Morshuis, M. Karperien, The use of peptides, aptamers, and variable domains of heavy chain only antibodies in tissue engineering and regenerative medicine, Acta Biomater. 170 (2023) 1–14.
[57] K.E. Johnson, T.A. Wilgus, Vascular endothelial growth factor and angiogenesis in the regulation of Cutaneous wound repair, Adv. Wound Care 3 (10) (2014) 647–661.
[58] L. Li, A. Zhou, Y. Wei, F. Liu, P. Li, R. Fang, L. Ma, S. Zhang, L. Wang, J. Liu, H. T. Richard, Y. Chen, H. Wang, S. Huang, Critical role of lncEPAT in coupling dysregulated EGFR pathway and histone H2A deubiquitination during glioblastoma tumorigenesis, Sci. Adv. 8 (40) (2022) eabn2571.
[59] A.K. Larsen, D. Ouaret, K. El Ouadrani, A. Petitprez, Targeting EGFR and VEGF(R) pathway cross-talk in tumor survival and angiogenesis, Pharmacology & Therapeutics 131 (1) (2011) 80–90.
[60] L. Niu, W. Yang, L. Duan, X. Wang, Y. Li, C. Xu, C. Liu, Y. Zhang, W. Zhou, J. Liu, Q. Zhao, Y. Han, L. Hong, D. Fan, Biological functions and theranostic potential of HMGB family members in human cancers, Therapeutic Advances in Medical Oncology 12 (2020) 1758835920970850.
[61] I.M. Evans, S.A. Kennedy, K. Paliashvili, T. Santra, M. Yamaji, R.C. Lovering, G. Britton, P. Frankel, W. Kolch, I.C. Zachary, Vascular endothelial growth factor (VEGF) promotes Assembly of the p130Cas interactome to drive endothelial Chemotactic signaling and angiogenesis, Mol. Cell. Proteomics 16 (2) (2017) 168–180.
[62] S.A. Tahir, S. Park, T.C. Thompson, Caveolin-1 regulates VEGF-stimulated angiogenic activities in prostate cancer and endothelial cells, Cancer Biol. Ther. 8 (23) (2009) 2286–2296.
[63] F. Biscetti, G. Straface, R. De Cristofaro, S. Lancellotti, P. Rizzo, V. Arena, E. Stigliano, G. Pecorini, K. Egashira, G. De Angelis, G. Ghirlanda, A. Flex, High-mobility group box-1 protein promotes angiogenesis after peripheral ischemia in diabetic mice through a VEGF-dependent mechanism, Diabetes 59 (6) (2010) 1496–1505.
[64] N. Silvestris, S. Tommasi, D. Petriella, D. Santini, E. Fistola, A. Russo, G. Numico, G. Tonini, E. Maiello, G. Colucci, The dark side of the Moon: the PI3K/PTEN/AKT pathway in Colorectal Carcinoma, Oncology 77 (Suppl. 1) (2010) 69–74.
[65] A.S. Mostafa, K.B. Selim, Synthesis and anticancer activity of new dihydropyrimidinone derivatives, Eur. J. Med. Chem. 156 (2018) 304–315.
[66] S. Liang, K. Sun, Y. Wang, S. Dong, C. Wang, L. Liu, Y. Wu, Role of Cyt-C/caspases-9,3, Bax/Bcl-2 and the FAS death receptor pathway in apoptosis induced by zinc oxide nanoparticles in human aortic endothelial cells and the protective effect by alpha-lipoic acid, Chem. Biol. Interact. 258 (2016) 40–51.
[67] W. Song, C.W. Fhu, K.H. Ang, C.H. Liu, N.A.B. Johari, D. Lio, S. Abraham, W. Hong, S.E. Moss, J. Greenwood, X. Wang, The fetal mouse metatarsal bone explant as a model of angiogenesis, Nat. Protoc. 10 (10) (2015) 1459–1473.
[68] H.S. Han, I. Jun, H.K. Seok, K.S. Lee, K. Lee, F. Witte, D. Mantovani, Y.C. Kim, S. Glyn-Jones, J.R. Edwards, Biodegradable Magnesium Alloys promote Angio-Osteogenesis to enhance bone repair, Adv. Sci. 7 (15) (2020) 2000800.